Monitoring of total and off-road NO$_x$ emissions from Canadian oil sands surface mining using the Ozone Monitoring Instrument

Chris A. McLinden[1,2], Debora Griffin[1], Vitali Fioletov[1], Junhua Zhang[1], Enrico Dammers[3], Cristen Adams[4,*], Mallory Loria[1,†], Nicolay Krotkov[5], and Lok N. Lamsal[6]

[1]Air Quality Research Division, Environment and Climate Change Canada, Toronto, Ontario, Canada
[2]Department of Physics and Engineering Physics, University of Saskatchewan, Saskatoon, Saskatchewan, Canada
[3]Climate, Air and Sustainability (CAS), Netherlands Organisation for Applied Scientific Research (TNO), Utrecht, the Netherlands
[4]Alberta Environment and Protected Areas, Edmonton, Alberta, Canada
[5]Laboratory for Atmospheric Chemistry and Dynamics, Goddard Space Flight Center, National Aeronautics and Space Administration, Greenbelt, MD, United States
[6]Goddard Earth Sciences Technology and Research, University of Maryland, Baltimore County, MD, United States
[*]Now at: Air Quality Research Division, Environment and Climate Change Canada, Toronto, Ontario, Canada
[†]Now at: Astronomy Research Centre, University of Victoria, Victoria, British Columbia, Canada

Correspondence: Chris McLinden (chris.mclinden@ec.gc.ca)

Abstract.

The oil sands in Alberta, Canada is a significant source of air pollution. Observations from the Ozone Monitoring Instrument (OMI) on the NASA Aura satellite have been used to quantify NO$_x$ emissions from the surface mining region of the oil sands. Two related emissions methods were utilized, one for point and one for area sources, where OMI vertical columns densities of NO$_2$ were combined with winds from a meteorological reanalysis and a two-dimensional exponentially-modified Gaussian (EMG) plume model. This work better connects the two (point and area) emissions methods, discusses the interpretation of fit parameters, and the ability of OMI (and other sensors) to resolve emissions between neighbouring sources.

The two methods employed, in good agreement with each other, indicated an increase in emissions from about 55 to 80 kt[NO$_2$]/yr between 2005–2011, and flat thereafter. Reported emissions were within 15% of reported emissions, consistent to within uncertainties. In an extension of this methodology, OMI observations were combined with reported point source emissions to derive the more uncertain emissions component from the large off-road mining fleet. These were found to make up about 60% of total NO$_x$ emissions, also consistent with reported emissions. The OMI-derived 0.9%/year increase in fleet emissions and the 5.5%/year increase in bitumen mined, generally a good proxy for fleet emissions, can be reconciled by considering the evolution of the mine fleet over this period. OMI is therefore able to track the transition from US EPA Tier 1 standards, through Tier 4 standards, to the present, and in so doing demonstrates the efficacy of this policy. Furthermore, this analysis shows that had the fleet remained at Tier 1 this source would currently be emitting an additional 40 kt[NO$_2$]/yr.

1 Introduction

The utilization of satellite observations of atmospheric composition for estimating or constraining emissions has expanded significantly in the past two decades (Streets et al., 2013) following improvements in sensor spatial resolution and precision, retrieval algorithms, and emissions methodologies. While satellite observations alone can often be used as proxies for emissions, at best they only contain information on the emitted mass of a pollutant, and not the rate of emission. To bridge this divide additional information on the dispersion (via atmospheric transport) and removal (though physical and chemical processes, if relevant) must be incorporated.

One common approach to obtaining "top-down" emissions estimates is through the use of 3D chemical transport or air quality models that simulate all relevant physical and chemical processes. Model emissions are adjusted such that the model-simulated and satellite observed quantities match to within some tolerance. The specifics of the approach may depend on several factors such as resolution of the model and lifetime of the pollutant, and vary from the straightforward mass balance (e.g. Martin et al., 2003) to a more formal Bayesian approach in which a cost function is minimized (Streets et al., 2013).

An alternative class of top-down methods have become increasingly common over the past decade in which satellite observations are paired with wind information to directly estimate emissions of air pollutants such as NO_x, SO_2, NH_3, CO, CH_4, and CO_2. This was done initially for point (or near-point) sources (Beirle et al., 2011; Pommier et al., 2013; Fioletov et al., 2015; Nassar et al., 2017; Varon et al., 2018; Dammers et al., 2019) but more recently for area sources (Fioletov et al., 2017; Beirle et al., 2019; McLinden et al., 2020; Fioletov et al., 2022; Liu et al., 2021; Wren et al., 2023; Fioletov et al., 2025). After several years of development, testing, refining, and validating, these methods are now being applied to emissions detection, verification and analysis (e.g. McLinden et al., 2016b; Ialongo et al., 2018; Goldberg et al., 2019a; McLinden et al., 2020).

In this work, direct methodologies such as these have been applied to surface mining within the Athabasca Oil Sands Region (AOSR), located just north of the community of Fort McMurray (57°N, 111.6°W)), in the Canadian province of Alberta (see Figure 1). The AOSR contains large deposits of bitumen, a viscous form of oil, which can be converted into a synthetic crude oil. In total, the AOSR is estimated to contain the equivalent of 170 billion barrels of oil, making it the second-largest reserve globally. In 2023, production from the AOSR was (the equivalent of) 3.4 million barrels of oil per day (mBPD) from bitumen, a number expected to rise to 4.0 mBPD by 2030 (Alberta Energy Regulator, 2023b).

Within the AOSR, about 20% of the proven reserves reside near the surface, at a depth of ∼75 m or less, and can be extracted through a process called surface mining. Surface mining first requires the removal of the overburden (muskeg and soil) in order to expose the deposit, followed by the extraction and transport of the raw bitumen to another on-site location for further processing to separate the bitumen from the sand and other impurities. For deeper deposits, in situ extraction methods must be employed in which steam is injected to reduce the bitumen viscosity so that it can be pumped to the surface. In either case, the bitumen is then converted into a synthetic crude oil through a process known as upgrading. Some facilities have on-site upgrading while others transport the bitumen elsewhere.

There are a number of environmental concerns associated with oil sands operations (e.g. Kelly et al., 2010), including water usage, deforestation (Rosa et al., 2017), greenhouse gas emissions (Rosa et al., 2017; Liggio et al., 2019; Wren et al., 2023),

and various potential environment effects to air, water, land, biota, and human health arising from the emission of pollutants. In particular, potential harmful effects on ecosystems from acidifying deposition (Makar et al., 2018), often referred to as cumulative effects. This refers to the environmental impact of past, present, and potentially future deposition, to the land and water. A comprehensive understanding of this impact, and how to mitigate it, requires an accurate knowledge of the emission rates of atmospheric pollutants (Galarneau et al., 2014; Gordon et al., 2015; Liggio et al., 2016; Li et al., 2017). Cumulative effects encompasses many pollutants, but in this work the focus are nitrogen oxides, NO_x (or the sum of NO and NO_2) which are emitted as a by-product of combustion.

The Ozone Monitoring Instrument (OMI) satellite sensor has been used previously to help understand the distributions of NO_2 and SO_2 (McLinden et al., 2012, 2016a, 2020) in the AOSR. These studies showed that a "hot-spot", or local enhancement, in NO_2 can be readily observed over the surface mining. Likewise, OMI has been utilized to quantify NO_x emissions with methods similar to that employed here from urban, industrial, and natural sources (Beirle et al., 2011; de Foy et al., 2014; Adams et al., 2019; Fioletov et al., 2022). This study builds on these to quantify NO_x emissions from AOSR surface mining using the now 19 year time series from OMI with the specific aim of understanding how they have evolved given its continued expansion and the changes in vehicle emissions standards over time.

2 Measurements and Methods

2.1 Emissions Data

This study is focused on quantifying NO_x emissions originating from a group of facilities withing a region in the northeast corner of the AOSR dominated by surface mining, defined here by a box bounded by latitudes of 56.80° and 57.46°N and longitudes of 112.0° and 110.7°W. This box (see Figures 1 and A1) contains all seven AOSR surface mining facilities, three relatively small in-situ facilities, as well as other minor NO_x emitters such as the community of Fort McKay (pop. <1,000). Bottom-up inventories (Zhang et al., 2018) suggest that oil sands surface mining facilities and activities are responsible for roughly 95% of total NO_x emissions within this area and so the term "surface mining region" is used here for convenience. Just south of this area is the community of Fort McMurray (pop. 70,000, 15+ km South), and further south still are numerous in-situ facilities (50+ km South).

Several sources of emissions information were used in this work. Annual emissions from point sources reported to the Canadian National Pollutant Release Inventory (NPRI) (Environment and Climate Change Canada, 2020) are available up to 2023. NPRI point source emissions are based on a variety of methods: some stacks employ continuous emissions monitoring systems (CEMS) (Alberta Government, 1998), others are based on engineering estimates, and some use a combination of both. The primary source of mine fleet emissions were created in accordance with the Environmental Protection and Enhancement Act (EPEA) (Alberta Environment and Parks, 2025) spanning 2010–2023, while those from the Cumulative Environmental Management Association (CEMA) for 2010 (Zhang et al., 2018) are also used for comparison. Related industrial activity data, including the total amount of oil sands mined on a monthly basis (Alberta Energy Regulator, 2023a), were helpful for interpretation and sampling corrections.
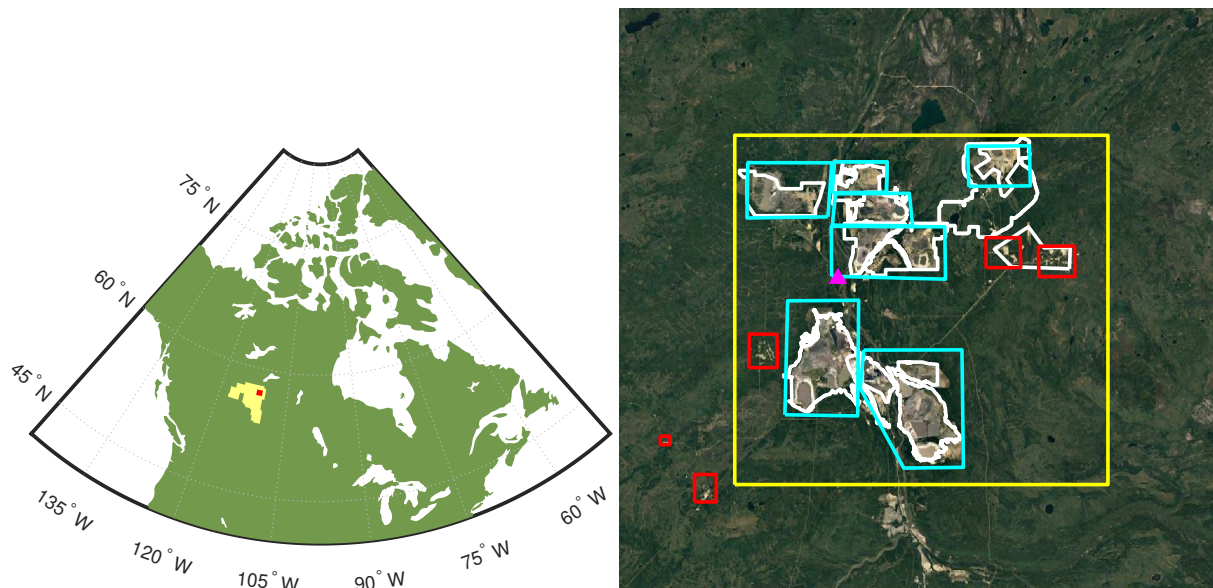
Figure 1. Left: Map of the Canada showing the Athabasca oil sands region (yellow) and the location of the surface mining area (red), which also corresponds to the area outlined by the yellow box in the right panel. Right: Map of the oil sands surface mining region (spanning 134 km N–S and 79 km E–W). The yellow box indicates the region over which emissions are added and assumed to be surface mining, although there are some minor emissions from in-situ facilities that also reside within the yellow box. The cyan boxes indicate surface mines, whereas the red boxes are smaller in-situ facilities. The magenta triangle shows the location of the Bertha Ganter – Fort McKay monitoring site, and the Fort Chipewyan site is 169 km due north of this. Map Data: Google, Image Landsat/Copernicius. © Google

Emissions of NO_x from surface mining occur primarily from two source types. The first is the off-road vehicle fleet com-
85 posed of large, diesel shovels and trucks that operate 24/7. Three of the seven mining operations also have large point sources, stack emissions, from the upgraders that convert the bitumen into a synthetic crude oil. The in-situ facilities also have stack emissions although these are quite modest ($< 5\%$) in comparison. The databases indicate that, in 2010, within the surface mining region, roughly 38 kt[NO_2/yr] originated from the suface mining offroad fleet, 29 kt[NO_2/yr] from surface mine point sources, and about 1–2 kt[NO_2/yr] from in situ point sources. All other sources are estimated to emit considerably less than 1
90 kt[NO_2/yr] and are therefore ignored.

2.2 OMI Observations

OMI is a Dutch–Finnish instrument launched in 2004 on the NASA Aura satellite (Levelt et al., 2006, 2018). OMI measures back-scattered sunlight in the UV–visible using a two-dimensional detector that measures simultaneously at 60 across-track positions. Its spatial resolution at nadir is 13×24 km^2 but it gets progressively worse at larger off-nadir angles. A blockage
95 beginning in 2007 -– the so-called "row anomaly" -– has meant some track positions are no longer reliable (Levelt et al., 2018; van Geffen et al., 2019). As of 2020 more than half of the across-track positions are affected.

Version 4.0 of the OMI NO_2 standard product (Krotkov et al., 2018; Lamsal et al., 2021) is used here. It, like many UV-visible NO_2 retrievals, uses a three-step approach to determine tropospheric NO_2 vertical column densities (VCDs) from measured spectra, where the tropospheric VCD represents the vertically-integrated number density between the surface and the tropopause.

The first step in the retrieval is a determination of the total absorption by NO_2, quantified in terms of a slant column density (SCD). The SCD represents the NO_2 number density integrated along the path of the sunlight through the atmosphere. Since OMI measures scattered light the path is complex and includes one or more scattering events and/or surface reflections. SCDs are derived through an analysis of the measured spectra by exploiting the difference in absorption at nearby wavelengths and involves a spectral fit of reference spectra, one of which being the NO_2 absorption cross-sections, to the measured spectra . The second step is the removal of the stratospheric component of the total SCD. This is accomplished using a complex high-pass filtering approach. The final step is a conversion of the remaining tropospheric SCD into a tropospheric VCD via an air mass factor (AMF) that accounts for the sensitivity of the instrument to NO_2 for a particular scene, where VCD=SCD/AMF. In practical terms, a multiple-scattering model is used to calculate AMFs (Palmer et al., 2001) to account for the complex path of light through the atmosphere. AMFs depend on factors such as solar and viewing geometry, the presence of clouds, scene reflectivity, and the vertical distribution of NO_2.

AMFs are one of the largest sources of uncertainty in NO_2 VCDs (Lorente et al., 2017). In the OMI NO_2 standard product (SP, version 4.0), model profiles at 1° resolution are used for the vertical distribution. As these are coarser than the individual OMI pixels, this acts to smooth the VCD distribution. To improve the effective spatial resolution, AMFs were recalculated using higher resolution inputs and more recent oil sands emissions (McLinden et al., 2014). These inputs include NO_2 profiles from the Global Environmental Multi-scale – Modelling Air quality and CHemistry (GEMMACH), discussed in section 2.3, and an annually-varying monthly-mean MODIS clear-sky reflectivity at 0.05° (Schaaf et al., 2002) smoothed to 15 km. Furthermore, snow pixels are identified using the Interactive Multisensor Snow and Ice Mapping System (Helfrich et al., 2007) which was found to be the snow product best suited for distinguishing between snow-free and snow-covered scenes (Cooper et al., 2018). When snow was detected, AMFs were then calculated using a MODIS-derived 15 km snow reflectivity as per McLinden et al. (2014).

OMI NO_2 VCDs were filtered as follows: track positions affected by the row anomaly are not used, and the track positions at the edge of the detector, 1–7 and 54–60 which correspond to the coarsest spatial resolution, are also removed. Note that pixels affected by the row anomaly change over the course of the mission which impacts both the data density and, as discussed below in Figure 3c, the effective spatial resolution. See Torres et al. (2018) for more information on the evolution of the row anomaly. Only observations made for solar zenith angles of 75° or less are retained. At a latitude of 57°N this removes the majority of data for the months of November to January. Note that a seasonal correction was developed to account for this in the determination of annual emissions (see section 2.4.4, below).

2.3 The GEM-MACH Air Quality Forecast Model

This study utilizes output from the Canadian Global Environmental Multi-scale - Modelling air quality and Chemistry (GEM-MACH) regional operational air quality forecast model (Moran et al., 2010; Pavlovic et al., 2016; Makar et al., 2017; Pendlebury et al., 2018) which covers most of North America. GEM-MACH is an on-line chemical transport module that is embedded within the ECCC weather forecast model. GEM-MACH was utilized as described in McLinden et al. (2014) where monthly-mean NO_2 profiles at 15 km $\times$ 15 km were computed for use in the AMF calculations. As discussed below in section 2.4.3, GEM-MACH was also used to better quantify the NO_2/NO_x ratio.

2.4 Satellite-derived Emissions

Emissions are derived using a direct approach in which wind information is paired with individual OMI NO_2 VCD observations. In this step, vertical profiles of the $u-$ and $v-$components of wind speed are obtained from the ECMWF (European Centre for Medium-Range Weather Forecasts) reanalyses, ERA-5 (Hersbach et al., 2020).

From here, two related emission algorithms are employed: one developed for isolated, near-point sources (Fioletov et al., 2015) and one for multiple or area sources (Fioletov et al., 2017). Both algorithms rely on a two-dimensional exponentially-modified Gaussian (EMG) plume function which translates the emissions into a spatial distribution. The functional form for the 2D EMG, provided in appendix B, is essentially a modified version of the traditional Gaussian plume with simple (e-fold) chemistry (Stockie, 2011) but is integrated in the vertical dimension and accounts for the finite size of the source and spatial resolution of the instrument. The EMG plume distribution varies with upwind/downwind and across-wind distance from a reference point that represents the location of the source, windspeed, and also depends on three parameters: pollutant mass, m, its effective lifetime τ, and a plume width parameter, σ. The emission rate, assuming a mass balance, is simply $E = m/\tau$. Henceforth the EMG will be described as a function of (E, τ, σ) for simplicity.

The effective lifetime describes the rate of decay of the pollutant due to chemical (e.g., conversion into other species) or physical (e.g., dry deposition) loss. It is well known that the lifetime of NO_x depends on NO_x-itself, and a recent study (Laughner and Cohen, 2019) elucidates this in the context of theoretical NO_x-lifetime curves for various volatile organic compound reactivity regimes. Previous studies using EMG-like functions found effective lifetimes of 2–5 hours by following the downwind decay of NO_2 VCDs (Beirle et al., 2011; de Foy et al., 2015; Lange et al., 2021).

The effective plume width (or spread) parameter, σ, is interpreted as a combination of a plume diffusion parameter, σ_{diff}, the spatial resolution of the satellite instrument, σ_{pixel}, and the physical size or extent or size of the source itself, σ_{size}. Given the Gaussian nature of the EMG, it is reasonable to assume that these are related through a functional form resembling,

$$\sigma^2 = \sigma_{\mathrm{diff}}^2 + \sigma_{\mathrm{pixel}}^2 + \sigma_{\mathrm{size}}^2. \tag{1}$$

Considering the physical extent of the oil sands, σ_{size} is expected to be tens of km. Similarly, given the OMI spatial resolution, σ_{pixel} should be on the order of 20 km. The remaining term, from equation (B4), is $\sigma_{\mathrm{diff}}^2 = \alpha \cdot y^\beta$ where y is the downwind distance, and $\alpha = 1.5$ km and $\beta = 1$ (Fioletov et al., 2015). Conventional Gaussian plume models use values more like $\alpha = 0.33$

km and $\beta = 0.86$ (Stockie, 2011). The larger value for α accounts for additional uncertainty in the wind downwind of the source. In the case of OMI, with its rather coarse resolution, decreasing α has virtually no impact on the fit.

The precise relationship between σ, σ_{diff}, σ_{size}, and σ_{pixel} was explored in appendix F using a simple model in which a collection of true-Gaussian plume point sources were used to simulate a near point source (of some radius σ_{size}) and smoothed to a specified satellite resolution (for pixel size σ_{pixel}). Fitting this combined distribution to an EMG allowed a relationship between these various terms to be established. Figure F1 shows σ has a dependence reminiscent of σ_{size}^2 and σ_{pixel}^2, and for small values of both, values less than 1 km which suggests σ_{diff} is small. Figure F1 will be used below to help interpret results. This further suggests that only for instruments with substantially higher spatial resolution than OMI, and likely even TROPOMI or TEMPO (Zoogman et al., 2017), would this σ_{diff} term need to be refined.

The EMG plume function is used in two ways. The first is an inverse mode where combined OMI-wind data are fit in order to derive (E, τ, σ). The second way is in a forward mode to predict the spatial distribution of VCDs (at an OMI-like spatial resolution) by prescribing winds and values for (E, τ, σ). The input emissions used for this forward mode can be those derived from OMI (in the inverse mode), in which case the intent is to 'reconstruct' the original OMI observations to test for consistency. Alternatively, a modified or even completely independent source of emissions, E, can be used, with τ and σ as derived from OMI, in order to examine the predicted spatial distribution of VCD (at OMI spatial resolution).

2.4.1 Point Source Method

The first emissions approach considered is the point source method of Fioletov et al. (2015), used previously to derive emissions of SO$_2$ (Fioletov et al., 2016; McLinden et al., 2020), NH$_3$ (Dammers et al., 2019), and NO$_x$ (Griffin et al., 2021). Observations from many OMI overpasses are combined using a rotation procedure in which all observations are re-positioned about a reference location according to their individual wind directions such that, after rotation, all observations share a common wind direction (Pommier et al., 2013). In other words, the upwind/downwind and cross-wind positions, relative to the reference location, of each observation is preserved. In this way multiple overpasses can be analyzed as a single, average plume. In this method values of (E, τ, σ) are determined that minimize the difference between the EMG plume function and the OMI observations in the rotated plume. Since τ and σ are non-linear parameters, a non-linear solver is used. A variation of this method is also used in which τ and σ are prescribed, thereby allowing E to be determined using a linear regression which is more stable and often means fewer observations are required. Details on the practical implementation of this method are given in appendix C.

2.4.2 Multi-Source Method

The second method, developed for multiple or area sources (Fioletov et al., 2017, 2022), was also employed. This is a complimentary approach to the point source method in that the same EMG plume function is used except here (τ, σ) are specified and emissions from multiple locations are solved for simultaneously. At each location an EMG basis function is generated for all OMI observations being used in the fit. The OMI VCDs are modelled as the sum of all EMG functions which represent the local sources, and a background term, which represent the NO$_2$ that would be present in the absence of local sources. The

background can be a simple constant offset, or allowed to vary linearly in latitude and longitude. A multi-linear regression is then performed which provides a set of emissions that minimize the difference between the OMI and modelled (or reconstructed) VCDs. Unlike the point source method, this fit is performed in the original latitude-longitude frame (i.e., not in the rotated frame) and a positive constraint is placed on the emissions.

In this multi-source method, the choice of emission locations is arbitrary. If the emission sources are well known then these locations can be used. Likewise, a grid of locations can be used when their spatial distribution is uncertain or complex. One aspect of this approach is that τ and σ must be specified. While the effective lifetime can be estimated from a model, there is a question as to how precisely to do this. An alternative approach, and the one adopted here, is to use the effective lifetime derived from the point source method. The choice of σ is not necessarily obvious since it encompasses multiple parameters, as indicated by equation 1. It should be chosen such that σ_{size} represents the physical size of the emissions. For a collection of point sources, then $\sigma_{\mathrm{size}} = 0$. For a grid representing an area source, σ_{size} should be on par with the grid spacing. Of course, this assumes σ_{OMI}, or at least $\sigma_{\mathrm{diff}}^2 + \sigma_{\mathrm{OMI}}^2$, is known. One method to estimate these other terms is to fit σ for a true point source as is discussed below. Additional information is provided in appendix D.

2.4.3 Other Considerations

One important parameter that must be specified is the altitude of the winds, where the altitude is chosen to represent the average height of the NO$_2$ plumes. As emissions are roughly proportional to wind speed, and wind speeds typically increase rapidly with height through the boundary layer, this also represents one of the larger sources of uncertainties. Previous studies used winds averaged over the lowest 500 m for urban, primarily vehicle (Goldberg et al., 2019a), emissions while another study used winds over the lowest 1 km (Fioletov et al., 2015).

In this work, wind heights are based on the observations from aircraft campaigns conducted in 2013 and 2018 which studied pollutant transformation downwind of the oil sands (Li et al., 2017; Liggio et al., 2019). These aircraft data indicated that NO$_x$ within plumes were found to reside at altitudes between the lowest altitudes sampled by the aircraft (100–300 m above the surface) and 800 m. In these same plumes, SO$_2$, which originates only from the upgrader stacks (e.g. McLinden et al., 2020), was found at 400–800 m. This indicates that NO$_x$ from the upgrader stacks is best represented at 400–800 m, while emissions from the fleet at 0–400 m. On this basis, and assuming roughly equal emissions from the stacks and the vehicles as suggested by the bottom-up inventory, winds, averaged between the surface and 800 m will be used for the majority of the analysis herein. Furthermore, an uncertainty of 100 m is assigned to the wind height, which translates into a difference in wind speed of roughly 10% since, in the vicinity of the oil sands, wind speeds on average were found to roughly double between the surface and 1000 m. For situations where fleet and stack emissions are treated separately, winds averaged over 0–400 and 400–800 m are used, respectively.

As OMI only observes NO$_2$ a correction must be applied to account for the missing NO. Typically this is done by estimating the NO$_x$/NO$_2$ concentration ratio and scaling the derived emissions by this. Previous studies often used more generic values of 1.3–1.4 (Beirle et al., 2011; Goldberg et al., 2019a). Here, a site-specific value was determined from the GEM-MACH model. The annual average surface mining concentration ratio for NO$_x$/NO$_2$, considering grid-boxes within a 40 km radius and using

Table 1. OMI NO$_x$ emissions uncertainty budget when considering three years of observations.

Error Category	Source	Uncertainty	
		Magnitude (%)	Type (R=Random, S=Systematic)
Air Mass Factor	all systematic sources	14	S
Data Filtering	Remove snow pixels	7	S
	±3 track positions	1	S
	cloud fraction ±0.1	3	S
EMG emissions fit	Fitting errors	5–10	R
	Fit downwind distance	3	S
	Fit box Width	4	S
	Different Methods	3	S
Winds	Wind speed and direction	6	R
	Wind height	10	S
NO$_x$/NO$_2$	NO$_x$/NO$_2$ ratio	8	S
TOTAL		20–25	%

the same monthly sampling pattern as OMI, is 1.50. The larger value is due in part to the inclusion of non-summertime chemistry where the photolysis of NO$_2$ is typically slower, particularly at higher latitudes.

230   However, using a single concentration ratio does not account for any spatial variability. Close to the actual site of the emissions this ratio can be larger as NO$_x$ is primarily emitted as NO (relatively less NO$_x$ is NO$_2$) while further downwind the opposite is true (relatively more NO$_x$ present as NO$_2$). This acts to skew the shape of the (rotated) plume thereby impacting the fit. Similar to Griffin et al. (2021), the GEM-MACH model is used to quantify the impact of this: VCDs of NO$_2$ and NO$_x$ for a year of simulations over the oil sands, along with model winds, are each fit to the EMG plume function using the point source

235 method. Taking the ratio of NO$_x$ to NO$_2$ emissions derived in this way reveals a ratio of 1.63, which is roughly 10% higher than the simple concentration ratio. This 10% difference is a systematic effect that should be largely independent of location provided emissions are from combustion. This value of 1.63 was used here. See appendix F for additional information.

2.4.4   Uncertainties

There are several sources of uncertainty that limit the accuracy and precision of these OMI-derived emissions. Table 1 shows a

240 breakdown, with each listed as a random or systematic sources of uncertainty, for the point source method. They are arranged under five categories – AMF, data filtering, the EMG fit, winds, and the NO$_x$/NO$_2$ ratio.

    Only systematic errors in AMFs are considered since random errors should largely cancel as multiple years of data are analyzed together. A previous study (McLinden et al., 2014) found systematic uncertainties to be 14% due to approximations

with how aerosols are handled and the use of a Lambertian surface albedo. Data filtering refers to what OMI data are included or excluded in the analysis for which different thresholds could be argued: exclusion of snow pixels, track position cut-off, which really denotes the maximum size of the pixels, and maximum cloud fraction. These are systematic effects that collectively represent an 8% uncertainty.

The EMG fit contributes a random uncertainty to emissions related to the quality of the fit itself, which varies from 5–10% depending on the amount of data used. Beyond that, there are small systematic effects when it comes to the spatial domain used in the fit itself, specifically the cross-wind, upwind and downwind distances. There is also a small uncertainty included here that reflects how different variants of the algorithm produce slightly different emissions.

From Section 2.4.3, a systematic error of 10% from using an incorrect wind height is reasonable. Also, random errors in wind speed and direction were estimated to be 6% from a previous study (McLinden et al., 2016b). The NO_x/NO_2 emission ratio used here is 1.63 as discussed in section 2.4.3. An 8% systematic uncertainty is assigned to this category, arrived at by considering the differences between the average of the aircraft measurements from Figure E3 and multiple years of GEM-MACH output.

There are also potential sources of bias due to the sampling of the OMI instrument: overpasses are only in the early afternoon, and there is an unequal distribution of observations throughout the year. The first of these is only an issue if there is a diurnal cycle in emissions. Hourly emissions of SO_2, co-emitted with NO_x, from the upgraders indicate no consistent difference in time of day emissions. Likewise, the heavy hauler fleet of trucks are used 24/7 and it is assumed there is no systematic diurnal variation in these emissions. High-resolution GEM-MACH forecasts assume flat NO_x emissions for both source types (Zhang et al., 2018). In addition, the fitting algorithm itself smooths the diurnal cycle impact to some extent as NO_x emitted before the overpass time is sampled downwind.

Any potential seasonality bias is largely eliminated using OMI observations from all months. Nonetheless, the SZA cutoff of $75°$ and the change in cloud cover with season means not all months contribute equally. The impact of this is assessed using monthly bitumen mining data (Alberta Energy Regulator, 2023a). Each OMI pixel is assigned a bitumen-mined value equal to its corresponding monthly total. An annual average bitumen-mined value was then calculated averaging over all pixel values, thereby capturing the OMI sampling, and these were then compared to the average assuming an equal weighting. The resultant bias is typically about 1–2%, with one year reaching 5%. This correction was applied directly to the OMI emissions. See appendix F for the time series and additional information.

Constructing an error budget for the multi-source method is more challenging, but it is argued here that it would be very similar since the largest contributors are systematic errors from the AMFs and winds, which would be common to both. As discussed below, fitted parameters from the point source method are used as inputs to the multi-source which also speaks to their connection. Given all this, and what was found to be a high degree of consistency in emissions as obtained from each method, this uncertainty budget is used for both approaches.

It is worth noting that the uncertainties derived here are smaller than that reported in other satellite-based NO_x emission studies. There are several reasons for this: (i) location-specific and temporally-resolved fitting parameters (τ and σ) , (ii) the

use of multiple years of data to reduce fit uncertainties, (iii) aircraft observations of real plumes providing more confidence in wind heights, and (iv) a location-specific and more detailed consideration of the NO_2/NO_x ratio.

3 NO_x Emissions from the Oil Sands

3.1 Surface Mining as a Point Source

An initial assessment of NO_x emissions for oil sands surface mining is made using the point source method. Here, a reference location of 55.06°N, 111.55°W is used as it is the location of the maximum in the mean OMI NO_2 VCD distribution, as shown in Figure 2a. Winds are taken as the average between the surface and 800 m (see section 2.4.3). Figure 2 shows a summary of the emissions procedure considering the entire OMI time series (2005–2024). These maps were created using a 2×2 km^2 grid and a 12 km oversampling radius (Fioletov et al., 2011). Panel (a) shows the mean NO_2 VCD along with an outline of the surface mines and the reference location. Panel (b) uses the same data as (a) but averaged in the rotated frame, as a function of downwind and cross-wind distance from the reference location. In this frame the reference location corresponds to (0,0). There is a clear plume-like feature that peaks just downwind of the reference location before it decays close to background some 100–150 km downwind. The peak value in the rotated frame is roughly 10–15% larger as compared to the original frame as a result of a greater cohesion in the distribution. Panel (d) shows the map that results from the non-linear fit of the individual VCD observations to the EMG plume function in the rotated frame, and it can be seem to capture the shape of the average plume in (b). The fit parameters are E= 69.7 ± 2.2 kt[NO_2]/yr, $\tau = 3.2 \pm 0.1$ hours, and $\sigma = 20.6 \pm 0.3$ km, where the uncertainties are statistical only, an indication of how well the EMG represents the OMI/wind observations. The overall uncertainty in the emissions would be roughly $\pm20\%$, from section 2.4.4.

The remaining panel, (c), shows the reconstructed VCD distribution as found by rotating the fitted values in panel (d) back to the original latitude-longitude co-ordinates. This generally resembles the mean OMI VCD map in panel (a) but has a smaller peak value and appears much more symmetric. This is a result of assuming all emissions originate from a single point, the reference location given by the triangle. Of course in reality emissions are spread out (see Figure 1) over a 60 km (N–S) $\times$ 40 km (E–W) expanse, which motives the use of the area or multi-source approach, below. The only reason why the reconstruction from panel (c) departs from a symmetrical pattern is that there is a preferred wind direction, out of the W and SW.

This approach is repeated, but now considering successive three-year time periods, where three years are combined to help ensure the stability of the non-linear, fitted parameters τ and σ, particularly in latter years when the row anomaly means less than half of all pixels are usable. An example of the mean and fitted VCDs plots, analogous to Figure 2 but for 2005–2007, is given in Figure C1. The fitted parameters are presented first, deferring any discussion of the emissions to section 2.4. Figure 3a shows the time series of the mass of the NO_2 enhancement. This represents the average mass of NO_2 that is present as a consequence of the surface mining NO_x emissions discussed in section 2.4. It is seen to increase with time, peaking mid-time-series ($\sim$2013), and them decreasing slightly. The dip in 2016 is attributed to the large forest fire just south of the surface mining in and around the community of Fort McMurray (Adams et al., 2019) that significantly impacted production throughout the month of May. Note that NO_x from the fires themselves originated 20 km south of the surface mines and two weeks later
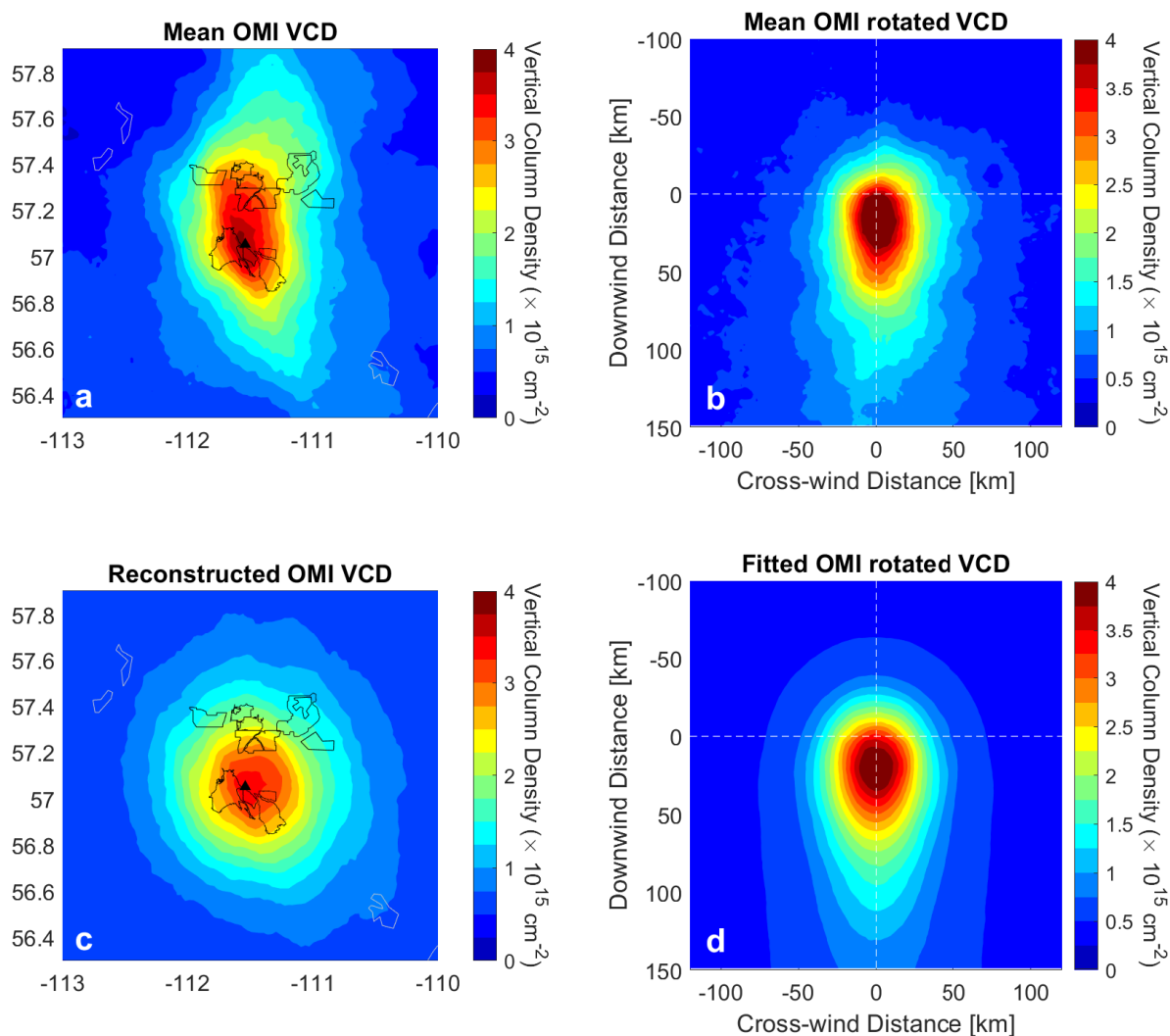
Figure 2. Summary of the point source emissions procedure using 2005–2022 OMI NO$_2$ VCDs. (a) Mean OMI VCD over the surface mining region of the oil sands. The black lines denote the different mining operations; (b) mean OMI VCD after rotation showing plume-like structure; (c) Reconstructed spatial distribution using EMG plume and fitted parameters; (d) Fit to rotated VCD using 2D EMG plume function, with fitted parameters of E=69.7 kt[NO$_2$]/yr, $\tau = 3.2$ hours, and $\sigma = 20.6$ km. The black triangle in the panels (a) and (c) show the reference location used in the emissions retrieval and corresponds to the (0, 0) point in panels (b) and (d).

approached the southernmost edge (MNP (Meyers Norris Penny), 2017). There are only one or two days where it is conceivable that there could be some misidentification of fire-NO$_x$ for oil sands but given its proximity and wind direction, these data tended to be filtered due to higher cloud fraction. There is no obvious sign that COVID-19 public health restrictions affected emissions

in the most recent years, consistent with the 2020–2023 production data remaining roughly constant compared with previous

315   years (Alberta Energy Regulator, 2023b). The increase in the 1-sigma fitting error bars (in all panels, a–c) reflects the decrease in the number of OMI pixels due to the onset and expansion of the row anomaly.

For comparison, the three-year running average of in-situ NO$_2$ volume mixing ratio (vmr) is also shown in Figure 3a. Here, the average from the Bertha Ganter – Fort McKay monitoring station, located between the northern and southern cluster of mines, is used but, subtracted from it, is the NO$_2$ from a background station at Fort Chipewyan, roughly 170 km to the North.

320   This difference in station values is used as the mass reflects an enhancement in NO$_2$ above background levels due to the local sources. While this simple comparison cannot be considered a validation, their general consistency provides confidence in the approach.

From Figure 3b, the effective lifetime displays some variation with time, between 2.7–3.9 hours. It is well known than NO$_2$ can impact the abundance of OH, and hence its own lifetime (Valin et al., 2013), and it is in this context that this is explored

325   further, below. Krol et al. (2024) also highlight the importance of not using a single lifetime for an accurate determinaton of emissions.

The variation of σ is shown in Figure 3c, where it is seen to increase from ~ 18 km in the mid-2000s to ~ 21 km by 2009 and with a smaller rate of increase to ~ 24 km near the end of the OMI record. This is broadly consistent with an expansion of the surface mining activities in the north, including new mining operations coming online, which effectively increase the

330   area of NO$_x$ emissions. Also shown is the average effective size of the OMI pixels used in the analysis, calculated here as the square-root of mean pixel area, and it is seen to increase slightly with time due to the expansion of the row anomaly, particularly through 2008–2011. While similar to the increase in σ, the magnitude of the increase in pixel size is much smaller. The link between pixel size and σ is discussed below. From Figure F1, 21 km pixels for a surface mining radius of 30 km, would predict a value for σ of about 21 km, consistent with that derived here.

335   These results can be contrasted with a previous study (McLinden et al., 2012) in which, between 2005–2011, the mass was seen to increase at a similar rate over this period but was a factor of 2–3 smaller. This is due primarily to the differences in AMF, where the former study used the VCDs as provided in the KNMI version 2 data product (Boersma et al., 2011). In that data product, the model simulated NO$_2$ profiles were for background conditions as it has no emissions in the AOSR (McLinden et al., 2014). Other differences are due to the data version and the more sophisticated fitting in this work. It is this difference in

340   fitting that also complicates any quantitative comparison between the fitted width parameters in these two studies.

In order to examine the variation in lifetime more thoroughly, an effective-VCD was derived using the mass from 3a (converted to molecules) and divided by an area taken to be $\pi\sigma_{\text{eff}}^2$, where σ_{eff} is the width parameter from 3c. This would peak mid- and end-time-series and be a minimum towards the early years. Note that such a quantity is not the mean VCD, but simple one that accounts for the changing spatial extent of the source with time. Plotting this effective lifetime vs effective VCD shows a

345   reasonably compact relationship, as shown in Figure 4, with a correlation coefficient of 0.78. For pure chemical loss of NO$_x$ via NO$_2$+OH, $[\text{OH}] = 1/(k_{\text{OH}+\text{NO}_2} \cdot \tau)$ can be used to estimate [OH], giving values between 5–8$\times 10^6$ molecules/cm^3, also shown in Figure 4. For the 2013 flight campaign in the oil sands, summertime OH was estimated at 10×10^6 molecules/cm^3 (Liggio et al., 2016). The 2013 value from this OMI analysis, 6×10^6 molecules/cm^3, is generally consistent since it considers
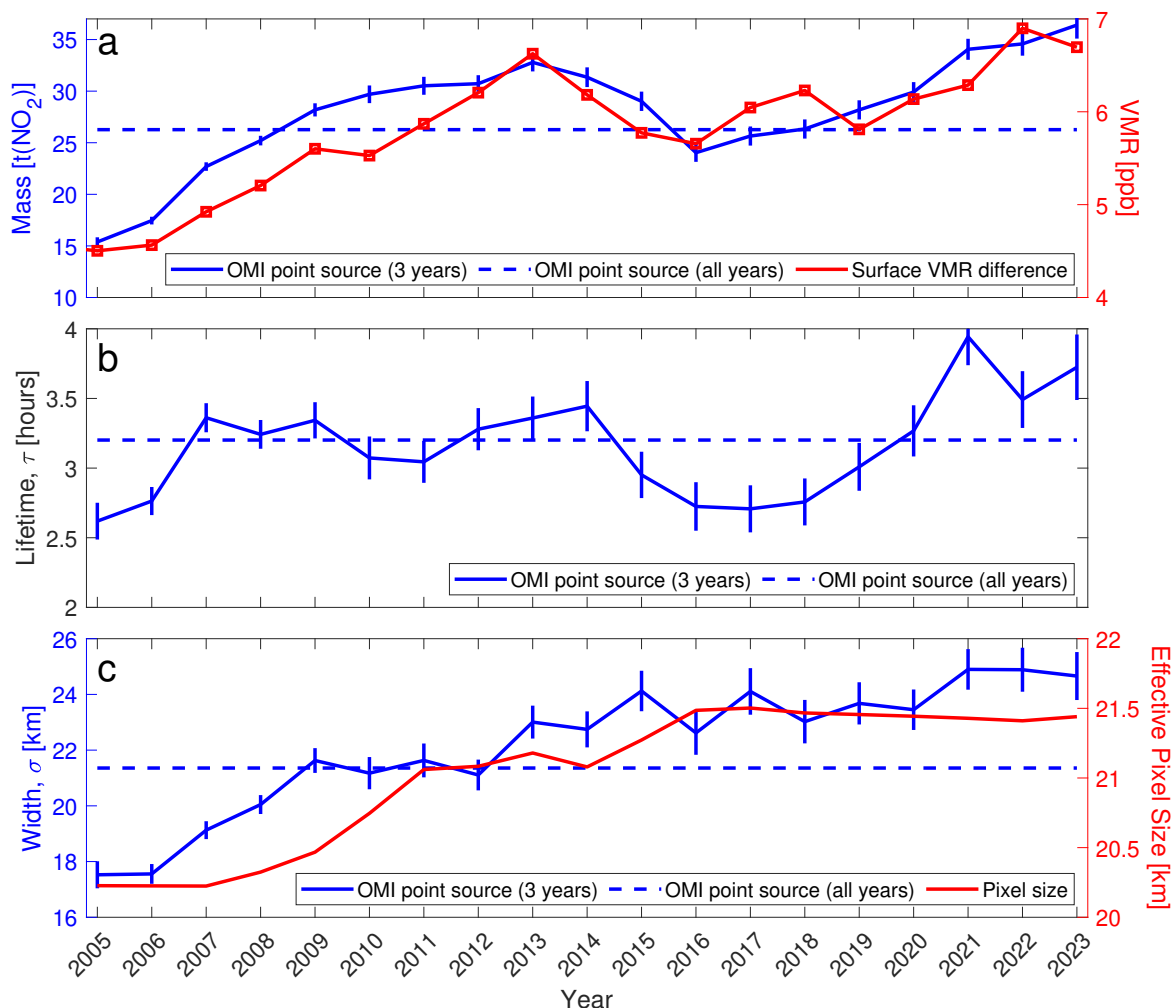
Figure 3. OMI point source emissions and parameter time series: (a) mass of the NO$_2$ enhancement and, for comparison, the difference in surface volume mixing ratio (vmr) between a surface mining and background site (see text), (b) effective lifetime of plume, and (c) plume width parameter and effective OMI pixel size, calculated as the square root of the mean of pixel area. All OMI-derived quantities are based on three-years of observations, such that, e.g., 2006 considered observations from 2005–2007, with the exception of 2005 which is based on two-years, 2005–2006.

all seasons (albeit weighted towards spring and summer) and wintertime values would be considerably smaller. This analysis suggests that at least some of the temporal variation of τ is real, and highlights the importance of using the period-specific τ when estimating emissions. Using the 2005–2023 mean τ (or some other constant value) could lead to a 10–15% additional error and skew the trend.
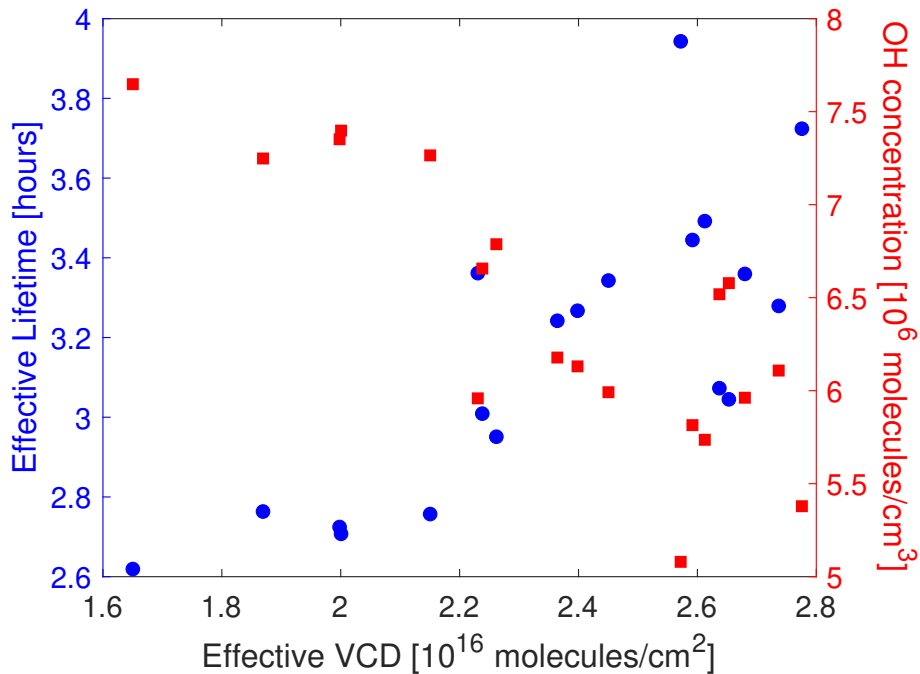
Figure 4. Relationship between effective VCD and lifetime and inferred OH concentration. Each point represents one three-year value from Figure 3.

3.2 Surface Mining as a collection of Point Sources

When quantifying emissions from a location where the spatial scale of the emissions is larger than σ (as is the case here), the
355   multi-source method may be more appropriate than the point source method. If the locations of the emissions are well known, then these can simply be specified; alternatively, a grid of potential source locations can be used. In this work both options were explored.

Initially, a grid of potential source locations covering the entire surface mining region is used. Initially an 8×8 km^2 grid is defined over an area of 250 km $\times$ 250 km centered on the surface mining. Each grid-box is treated as a (potential) point source,
360   analogous to the approach used in Fioletov et al. (2017). As discussed in section 2.4 and appendix D, emissions are derived for each grid-box such that their combined VCDs match the OMI observations. The positive constraint ensures most of these fitted values, and hence emissions, are zero.

In this approach σ and τ must be specified. Here τ is taken from the point-source analysis in Figure 3(b) and used for all individual sources. This is a simplification as it was already demonstrated in Figure 4 that τ depends on VCD, and hence local
365   emissions. It is argued here that this will be a secondary effect since (i) plumes from individual sources will frequently overlap due their proximity and the coarse spatial resolution of OMI, and (ii) significant cancellation of errors since the point-source

lifetime used was for the combination of all local sources, small and large. In the future, when isolating individual sources is the goal, it would be worthwhile to explore a parametrization which might account for this dependency.

Determining a value for σ is not as straightforward. The reason for this is because σ, as derived above, has embedded within it the spatial scale of the entire surface mining source (that is, the σ_{size} term in equation 1). Following the discussion in section 2.4, additional insight into how OMI views a point-source was obtained by analysing a different location, one which is more of a true point source. For this purpose, the Poplar River Power Station (NPRI ID 2079), a coal-burning power plant located in southernmost Saskatchewan (49.05°N, 105.49°W), was considered. Average reported emissions over the 2005–2020 period are 13.4 kt[NO_2]/yr, where OMI finds 11.5 kt[NO_2]/yr, suggesting a reliable fit. From this analysis a σ of 11 km was derived. This can be compared with the value from Figure F1 which, for $\sigma_{pixel} = 21$ km and $\sigma_{size} = 0$, yields a value of about 13 km, which is generally consistent. A value of $\sigma_{pixel} = 11$ km is used for the multi-source method.

Initially all OMI observations spanning 2005–2024 are analyzed together and so a value of $\tau = 3.2$ hours (see Figure 2) is used. Performing the multi-linear fit provides a grid of retrieved NO_x emissions. A comparison of the mean VCD map with the reconstruction using these retrieved gridded emissions is given in Figure 5a–b. The multi-source reconstruction now closely resembles the observations, and is much more realistic than the point source reconstruction from Figure 2d. The map of retrieved, gridded emissions used for Figure 5b is shown in Figure 6a. The emissions map shows large values over the surface mines, as expected, with the largest corresponding to the upgrader at the Syncrude-Mildred Lake and Suncor facilities. Total surface mining emissions, calculated by summing grid-boxes within the rectangle shown, are 62 kt[NO_2]/yr. Outside of this box, other small but non-zero emissions can be seen. Some of these correspond to known NO_x sources such as the city of Fort McMurray, in-situ mining operations, and other small non-oil and gas related sources. Some of the small but non-zero emissions retrieved are likely the result of systematic biases in the VCDs.

This retrieval grid is 31×31, totalling 961 grid-boxes. An important issue is the degree of independence of each box. One would not expect OMI, with its ∼21 km pixels, to be able to resolve emissions on an 8×8 km^2 grid. The multi-source method is based on EMG plume functions which serve as the basis functions in the multi-linear regression, and the extent to which they are correlated can be used to help determine the ability of OMI to spatially resolve emissions. At a distance of 8 km, neighbouring OMI NO_2 plume functions have a correlation of 0.92. Given uncertainties in the data and approximations of the method, this confirms that OMI is unable to disentangle them. A more reasonable correlation threshold is 0.5, below which individual sources can be resolved. This is explored further in appendix F, where Figure F2 shows how achieving this 0.5 threshold separation distance, z_{min}, varies with σ, and to a lesser extent, τ. For OMI NO_2, it was found that sources must be separated by about 22 km.

The minimum distance required to distinguish between neighbouring emissions concept is very important for satellite emissions monitoring. An expression relating z_{min} directly to satellite resolution, σ_{pixel}, can be estimated by combining Figures F1 and F2. The result is shown in Figure 7. Estimates for several satellite data products are shown. While longer-lived species tend to require a slightly larger separation, the main driver is spatial resolution. This figure suggests TROPOMI and TEMPO (Zoogman et al., 2017) are able to resolve NO_x emissions sources that are ∼9 and 7 km apart, respectively. This approach does not account for real data characteristics, source strength (and relative strength of the two sources), and quantity of data
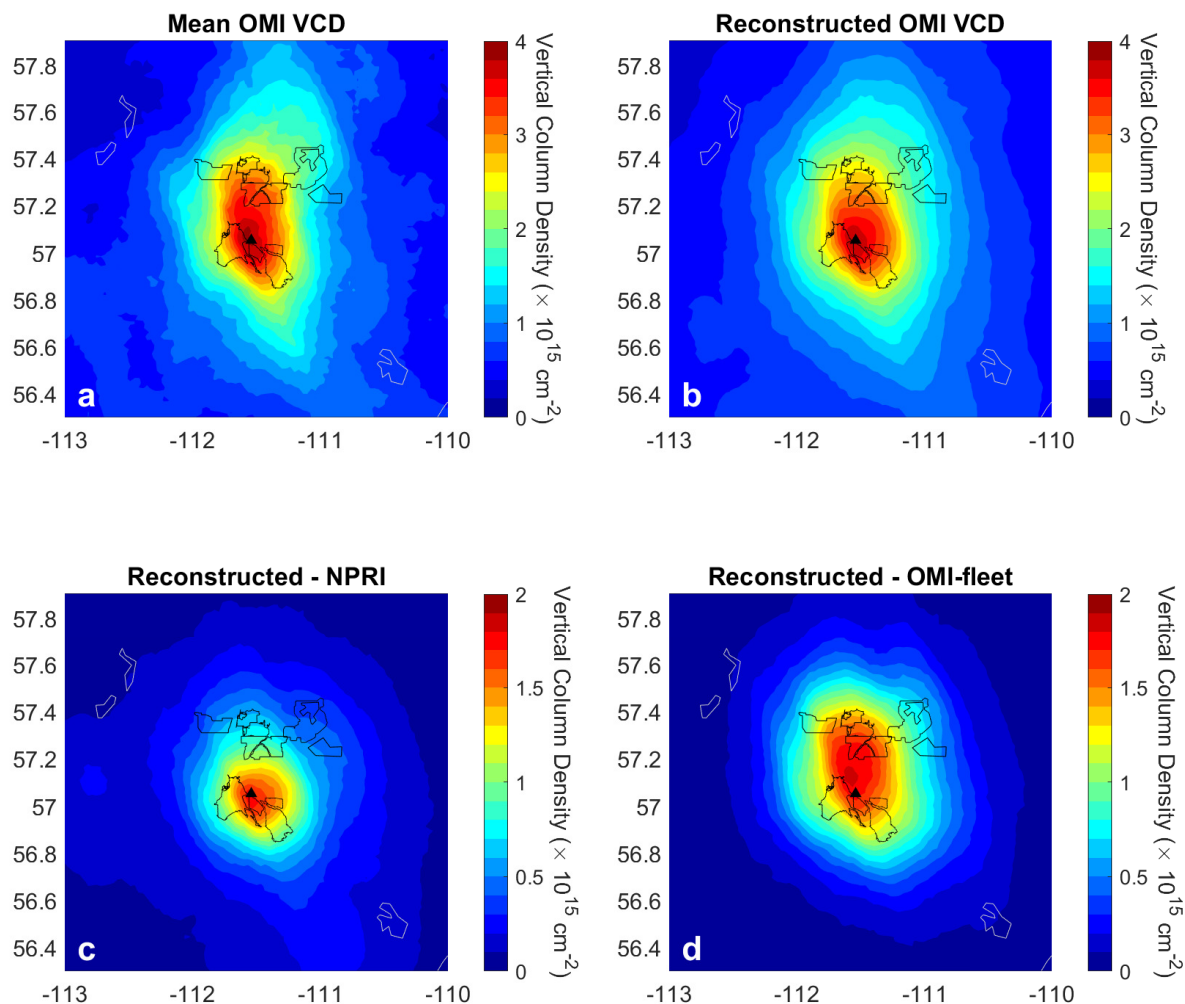
Figure 5. Summary of the multi source emissions retrieval using 2005-2020 OMI NO$_2$ VCDs. (a) Mean OMI VCD over the surface mining region of the oil sands. The black lines denote the different mining operations (this panel is the same as Figure 2a); (b) Reconstructed spatial distribution using the gridded emissions from Figure 6b. Panels (c) and (d) are the VCDs reconstructed using emissions from the NPRI point source database and OMI-derived area fleet emissions, also from Figure 6b. Note that the background is omitted from panels (b) and (c).

used. One might also argue that a correlation coefficient threshold of 0.5 is too stringent, and that perhaps 0.7 might be more appropriate.

The spatial scale of the individual surface mines is 5–20 km but they often are separated by little or no distance. It is on this basis, albeit with one exception in appendix D where this is explored further, OMI emissions derived from the multi-source

405
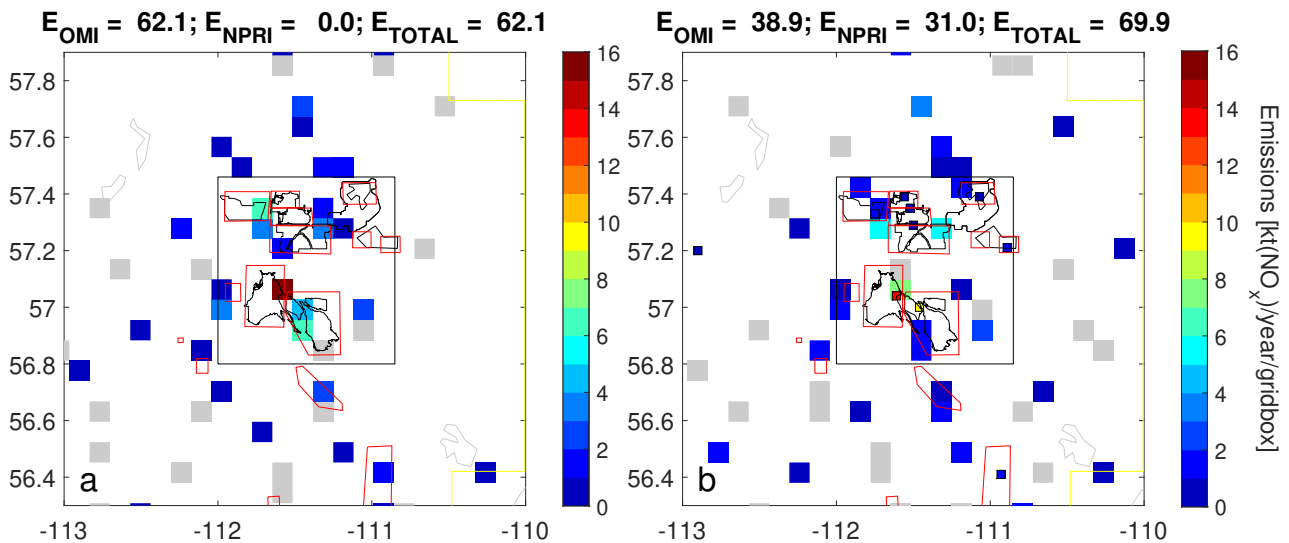
Figure 6. (a) OMI-derived NO_x emissions retrieved on an 8×8 km^2 grid using the multi-source method. These emissions represent the total of point and area sources. (b) as (a) but when point source emissions from the NPRI database, totalling 30.6 kt[NO_2]/yr, are specified. These gridded emissions represent area emissions only. Gray boxes represent retrieved emissions between 0 and 0.5 kt[NO_2]/yr. In (a) the total emissions within the box are 63.5 kt[NO_2]/yr; in (b) the total is 69.9 kt[NO_2]/yr, where 30.4 kt[NO_2]/yr were specified and the remaining 39.5 kt[NO_2]/yr were derived from the multi-source method.

method were simply summed over the surface-mining box. It is noted that TROPOMI, with its superior spatial resolution, should be able to separate out emissions for the majority of these mines.

An alternative implementation of the multi source method was used to derive vehicle fleet emissions. Recall that NO_x is primarily emitted by point sources, or stacks, and the off-road vehicle fleet. Some of the stack emissions make use of CEMS, and overall stack emissions are believed to be well known. Therefore, if the contribution to the OMI observations from the stacks can be removed, the remainder, from the fleet, can be fit using the same approach as above. This requires an initial step in which VCDs are reconstructed for each OMI observation, assuming stack emissions from NPRI, with these then subtracted from the actual OMI VCDs. This approach also allows an additional refinement as the height of the winds used for the prescribed stack emissions (400–800 m) can be different from those used to derive the off-road fleet emissions (0–400 m).

In practice this was done by first taking the NPRI emissions in the region, averaged over 2005–2020, and using these to reconstruct VCDs as shown in Figure 5c. The peak over the southern mines reflects the larger emissions from the two upgraders separated by about 10 km. These VCDs were then subtracted from the OMI observations, and the remainder used in the multi-source retrieval. The reconstructed total VCDs, those from the multi-source added to the NPRI VCDs from Figure 5c, are virtually identical to the that from Figure 5b and so it is not shown. Figure 5d shows the VCD reconstructed considering only the retrieved emissions which are attributed to the mine fleet. This VCD distribution are more homogeneous through the area, reflecting the more diffuse nature of this source.
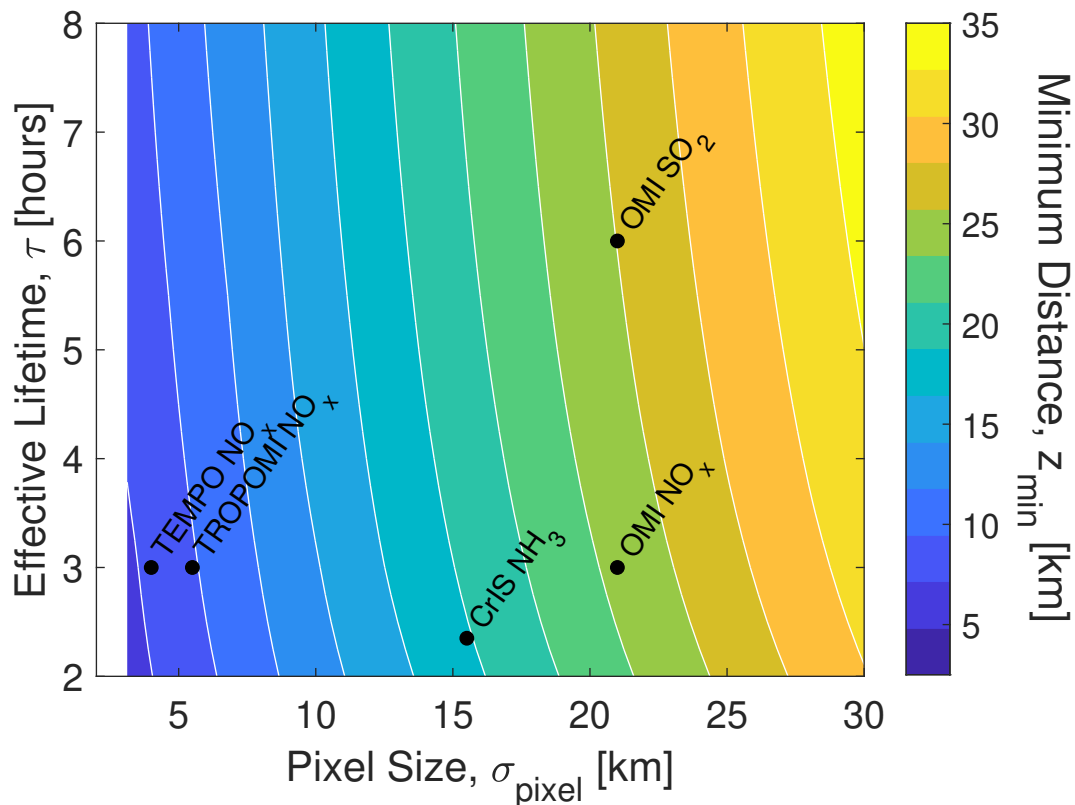
Figure 7. Minimum distance required to distinguish between two point sources as a function of satellite pixel resolution and effective lifetime. Values for several satellite emissions data products are also denoted.

The corresponding emissions map is shown in Figure 6b, where the small squares represent the prescribed NPRI point source emissions, and the grid box values are the retrieved (fleet) emissions. Total (point+fleet) emissions for the two methods differ due primarily to how the wind height is handled. Had the same winds been used in both, then the totals would be the same (to within 0.1–0.2 kt[NO_2]/yr) and one could have obtained the same result by simply subtracting the NPRI total from that in Figure 5a.

Two more variants of this method are considered. Here, instead of a grid, potential source locations are limited to known emissions sites, including industry and the city of Fort McMurray. The resultant emissions maps are shown in Figure 8. The squares reflect the emissions retrieved from each location. No attempt was made to account for the spatial scale of the mining operation; rather each was treated as a point source. As can be seen, the emissions maps are similar overall to the grid approach in both spatial distribution and surface mining total.
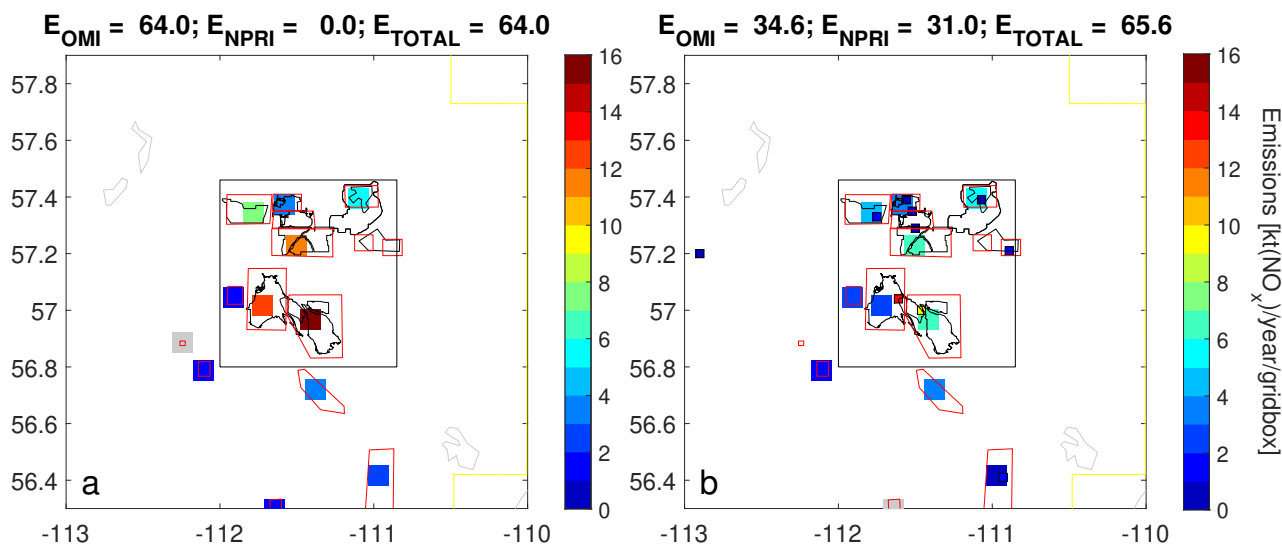
Figure 8. (a) OMI-derived NO_x emissions retrieved using the multi-source method where emissions locations are assigned to the centre of mining facilitues. These emissions represent the total of point and area sources. (b) as (a) but when point source emissions from the NPRI database, totalling 30.6 kt[NO_2]/yr, are specified. In (a) the total emissions within the box are 65.6 kt[NO_2]/yr; in (b) the total is 66.3 kt[NO_2]/yr, where 30.4 kt[NO_2]/yr were specified and the remaining 35.9 kt[NO_2]/yr were derived from the multi-source method.

3.3 Emissions Time Series

As with the point source method, emissions using the multi-source approach were also derived considering three-year time increments and using the effective lifetime time series from Figure 3b. Maps of average VCD maps and their reconstructions are shown in Figures D2 and D3, respectively. The emissions time series is shown in Figure 9.

Several variations of the multi-source were utilized, analogous to what was discussed in section 3.2. A summary of these are given in Table E1. Considering these together with the point source results shows relatively little variation amongst them, typically a few percent with the largest being 15% for a single 3–year periods. Based on this and the difficulty in determining which method is 'best' it was decided to take the mean of several methods, according to Table E1), as the final emissions value, with their variability taken as a measure of uncertainty.

Emissions are found to steadily increase over the OMI record from about 55 to 80 kt[NO_2]/yr as seen in Figure 9a between 2005 and 2010, remain roughly flat thereafter. Comparing total NO_x emissions, there is a good overall agreement between OMI and the bottom-up estimates. The bottom-up values are consistently 0–15 kt[NO_2]/yr smaller, but within the OMI uncertainties. As the time period over which the NO_x emissions were found to increase (2007-2011) generally corresponds to the main expansion of the OMI row anomaly, emissions over the entire time series were recalculated but restricted only to track positions that were unaffected by the anomaly over the entirety of the mission to date. Considering the previous criteria of excluding pixels near the edge of the detector due to their coarse spatial resolution, only track position between 8 and 23 were considered
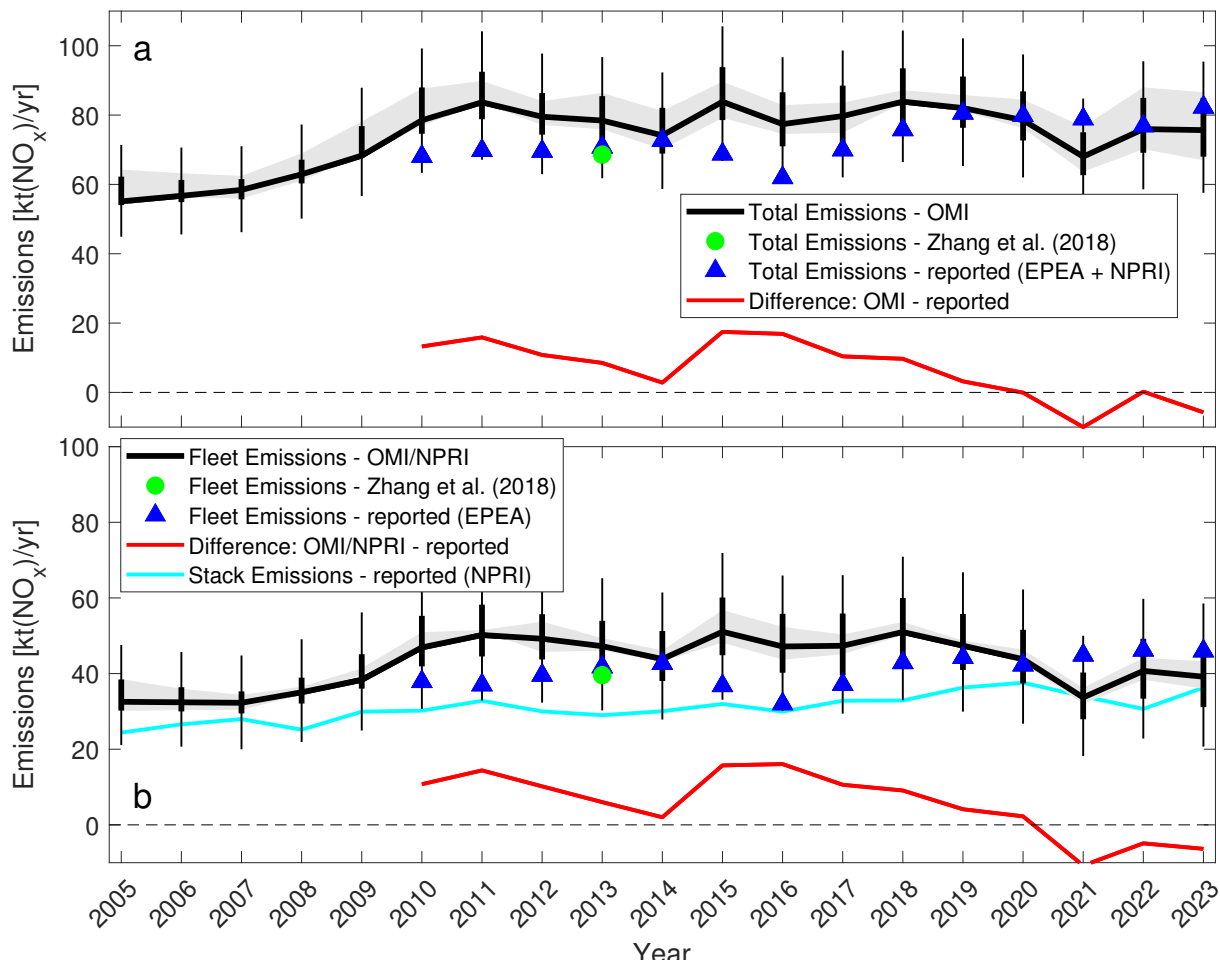
Figure 9. Comparison of reported and OMI-derived NO$_x$ emissions for (a) total and (b) fleet in the oil sands surface mining region. Thick error bars represent the random uncertainty and thin error bars represent total (random and systematic) uncertainty. The shading indicates the variability among the various methods for deriving emissions (and is included in the total uncertainty).

for this sensitivity study. Emissions calculated in his way were found to be minimally impacted, reaching roughly 3 kt[NO$_2$]/yr in 2007, well below the calculated precision, and not changing the overall time series picture.

450   Fleet emissions, as derived by prescribing stack emissions, are shown in Figure 9b. These generally follow the total emissions since the stack emissions only display a modest increase with time. The magnitude of the fleet emissions uncertainties are taken to be the same as that from the total emissions in Figure 9a. Fleet emissions were found to comprise about 60% of the total emissions. Neither reported nor satellite emissions show much variation over the 2010–2023 period for which both are available.
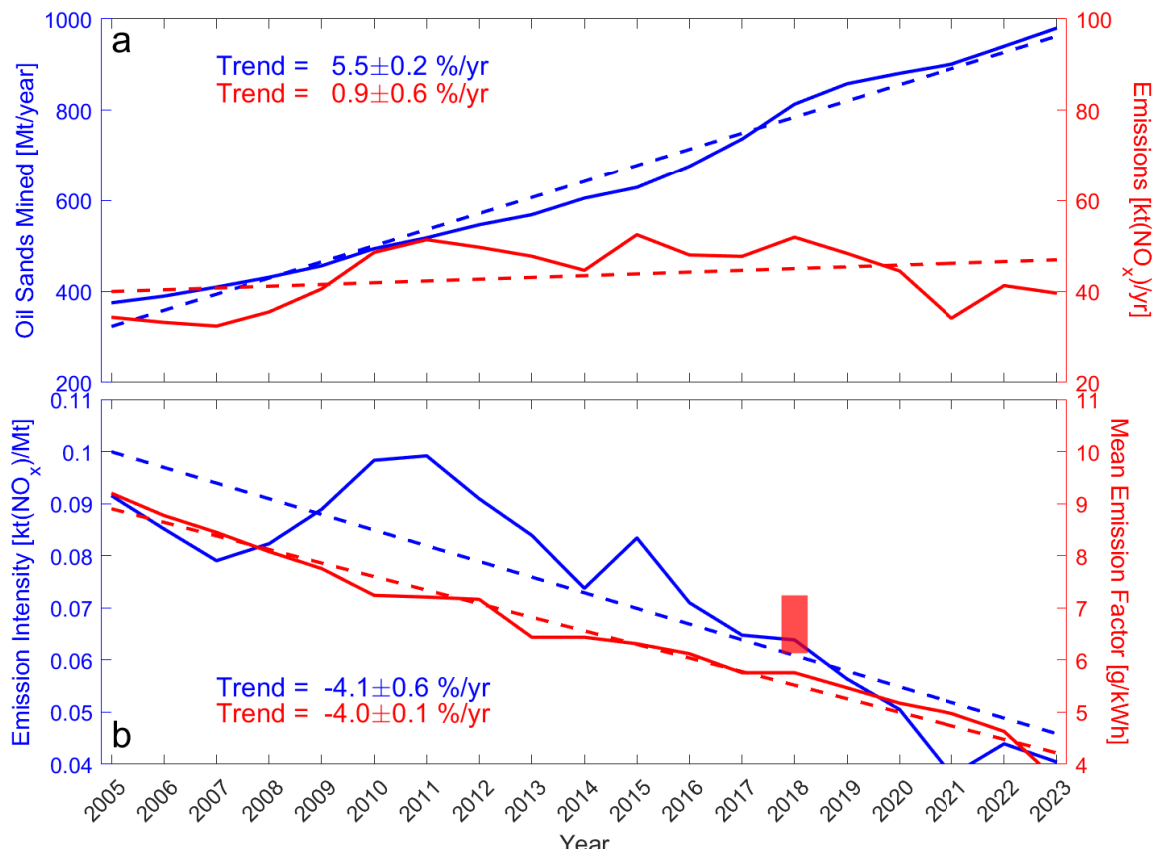
Figure 10. (a) Time series of mass of oil sands mined and fleet emissions from OMI. Dashed lines are linear trend lines, with the calculated trends indicated. (b) Emission intensity (defined as the ratio of fleet emissions to oilsands mined) and an estimated mean emission factor (see text). The shaded red bar show an estimate of the mean emission factor using reported fleet data.

4   Discussion

As can be seen in Figure 10a, the average rate of increase in fleet emissions is 1.3%/year since 2005, with the bulk of the increase occurring 2005–2011. Yet the rate of increase in the mass of oil sands mined, which is generally considered a reasonable proxy for fleet emissions since they must transport the bitumen from the mine to the separation facility, is considerably larger. This apparent discrepancy may be reconciled by considering the evolving standards as the Canadian vehicle NO_x emissions transitioned from unregulated (Tier 0) to present-day standards (Tier 4i/4) (Environment Protection Agency, 2016). As part of an agreement with the US, Canada adopted the EPA Tier 1 standard for heavy-duty, non-road vehicles (9.2 g[NO_x]/kWh) in 2000, the Tier 2 standard (6.4 g[NO_x]/kWh) in 2006, and then the Tier 4 standard (3.5 g[NO_x]/kWh) in 2012. There were no Tier 3 standards for this class of vehicle. Lower tier trucks could still be used as these stricter regulations were phased in, but
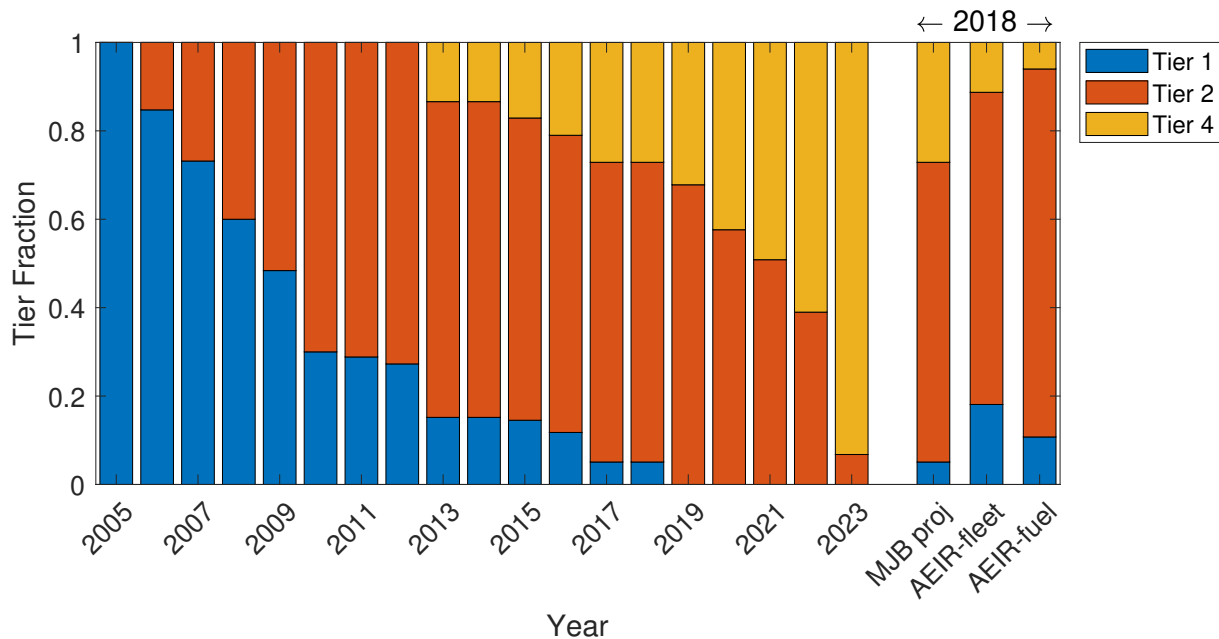
Figure 11. Composition of mine fleet according to emissions tier, shown as a cumulative fraction. The time series shows projections from the M.J. Bradley & Associates (2008) study for large (> 750 hp), diesel vehicles. The three on the right compare 2018 projected values with the 2018 AEIR fleet report, total vehicles and fuel consumed.

any new or replacement engines were required to comply with the standard of the time. With a typical engine lifetime of 12
465   years, the benefits of Tier 4 regulations will not be fully realized until the late-2020s (M.J. Bradley & Associates, 2008).

An emission intensity metric is defined here as the mass of NO_x emitted from the mining fleet per unit mass of mined oil sands, and this is shown in Figure 10b. It is seen to decrease at 3.8%/year. To contrast this with an expected decline, the composition of the vehicle fleet is required. Unfortunately, it was only in 2018 as part of the new Alberta Emissions Inventory Reporting Program (AEIR) that industry was required to report on fleet composition. While useful as a snapshot, this means
470   there is no direct information on fleet evolution over the study period.

One alternative is a study delivered to Environment and Climate Change Canada in 2006 projecting the make-up of the mine fleet going forward (M.J. Bradley & Associates, 2008). Their projected mine fleet composition is shown in Figure 11. This study predicted the largest growth between 2005 and 2010 where total vehicles increased from about 200 to 500, before leveling off at 600. This is the reason for the rapid increase in Tier 2 fraction. For comparison the AEIR data indicate a fleet size
475   of 730 large (> 750 hp) trucks in 2018. A comparison with AEIR reported tier fractions is also shown in Figure 11, where the weighting was done using total vehicles as a function of tier as well as fuel consumed by tier. There is general agreement with the projections, with tier 2 vehicles composing the majority. One difference is the fraction of tier 1 vs. tier 4, with there being fewer tier 4 vehicles than projected. Note that one large facility in the AEIR did not report which tier their vehicles belonged to and so these trucks were excluded from this analysis.

As a second alternative, a simple model was constructed beginning with 205 Tier 1 trucks in 2005. Trucks were increased at the same rate as total bitumen mined, with a fraction of existing trucks being replaced each year with ones at the current tier. Assuming a 12 year lifetime (M.J. Bradley & Associates, 2008), where for simplicity lifetime is taken as an e-fold such that 8.0% of trucks (or engines) were replaced each year. As suggested by the bitumen mined time series in Figure 10a, the total trucks increased steadily and doubled over the timeframe considered. The largest difference between this approach and the M.J. Bradley & Associates (2008) and AEIR data being the difference in Tier 2 truck fraction.

While the 730 large (> 750 hP) diesel trucks from the 2018 AEIR mine fleet report make up less than half of the 1610 total vehicles listed in the report, they accounted for 92% of the fuel consumed and so would also be responsible for the large majority of NO_x emissions. Overall, the AEIR total number of trucks, and the breakdown among the tiers, agree better with the projections. Nonetheless, the model remains a useful sensitivity study.

Assuming each truck uses the same amount of fuel and emits according to its standard, the weighted average emission factor can be computed for the projected fleet compositions. This was done by weighting the Tier 1/2/4 emission standard (9.2/6.4/3.5 g[NO_x]/kWh) with the fractions from Figure 11. Thus 2005 would have a value of 9.2 since it is entirely Tier 1, and 2006 would be slightly smaller since it is about 85% Tier 1 and 15% Tier 2. This metric, from Figure 10b, changes at -4%/year, a decrease that is essentially the same as that for the emissions intensity. In 2018, the emission intensity as defined above has declined by about 31% since 2005, and the mean emission factor using the fleeted projections has declined by 46%. These can be compared with the change in AEIR mean emission factor, assuming an initial value of 9.2 g/kWh, the Tier 1 NO_x standard. A decline of 21–31% is calculated, with the range depending on whether total vehicles or total fuel consumed was used to weight the mean.

Figure 10b suggests that the efficacy of the EPA emissions standards, at least in the case of the oil sands fleet, adopted by Canada are effective at or close to the level expected. Considering Figure 10b further, had emission intensities remaining constant at 2005 levels, with 2005 being the final year of Tier 1 standards, and increased with oil sands mined (5.6%/yr) instead of that observed (1.3%/yr), the fleet emissions reduction brought about from the adoption of Tier 2 and later Tier 4 standards, relative to Tier 1 is roughly 40 kt[NO_2]/yr in 2023. To put this into context, a value of 40 kt[NO_2]/yr is comparable to that emitted from an urban area (minus local industry) of 5M people using an approximate value for a per-capita rate of emissions of 7 kt[NO_2]/yr/(1M people) (Fioletov et al., 2022), or not quite half the roughly 100 kt[NO_2]/yr emitted from the Greater Toronto Area (Goldberg et al., 2019b) in the summer. Over the past 19 years, this amounts to roughly 400 kt[NO_2] less NO_x being emitted as a result.

The multi-source method can also be used to examine emission scenarios. For example, the impact on the average NO_2 VCD distribution due to a 20% reduction in fleet emissions or the opening of a new operation emitting 15 kt[NO_2]/yr could readily be evaluated. This is demonstrated in Figure 12 by comparing NO_2 VCD maps calculated using 2022–2024 OMI-derived fleet and NPRI emissions to VCDs derived using these fleet emissions increased by 50% as might be expected for Tier 1 vehicles. In order words, Figure 12b represents the scenario avoided by implementing Tier 2 and later Tier 4 standards.
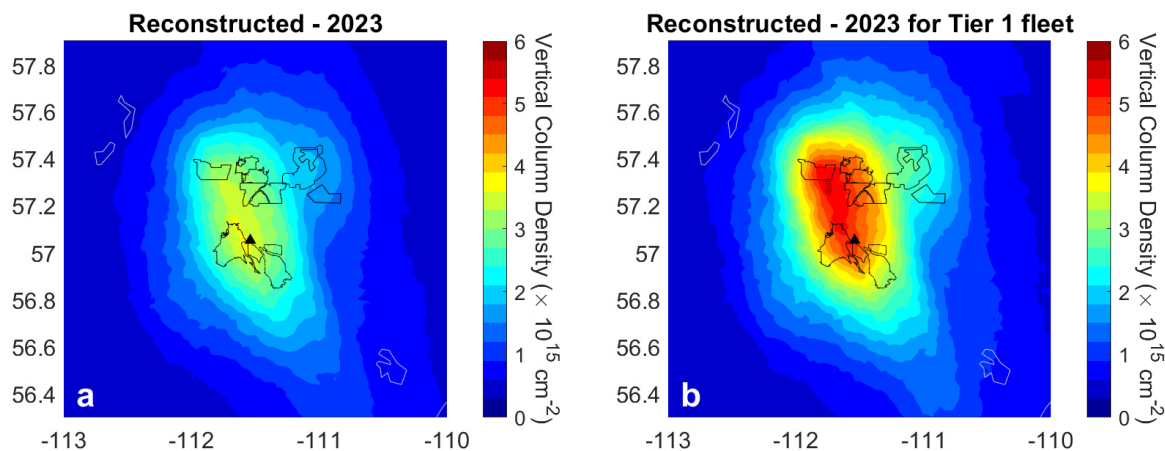
Figure 12. (a) Reconstructed 2023 NO$_2$ VCD map using OMI-derived fleet emissions and NPRI point source emissions. (b) As (a) but with fleet emissions doubled to approximate expected VCD distribution assuming Tier 1 emission standards. Note the colourbar range here is different as compared with previous figures.

5   Summary and Conclusions

OMI observations of NO$_2$ tropospheric VCD were used to quantify NO$_x$ emissions from the surface mining region of the Canadian oil sands between 2005 and 2024. Two different, though related, emissions algorithms were found to give very similar results. One assumes all emissions emanate from a single (near) point source, whereas the other treats the area as multiple point sources, or an area sources. These methods both utilize wind speed and direction from a meteorological reanalysis and a two-dimensional exponentially-modified Gaussian (EMG) plume model.

OMI-derived emissions were found to increase from 55 to 80 kt[NO$_2$]/yr between 2005–2011, and then remain roughly flat afterwards. These were found to be within 15% of reported emissions, but given a 20% uncertainty in the OMI emissions, this difference is not significant. In an additional variation of this methodology, OMI observations were combined with reported point source emissions to derive the more uncertain emissions component from the large off-road (heavy-hauler) mining fleet. These were found to make up about 60% of total NO$_x$ emissions, consistent with about 55% from reported emissions. The 0.9%/year increase from this source and the 5.5%/year increase in bitumen mined, generally a good proxy for fleet emissions, can be reconciled by considering the evolution of the mine fleet over this period. OMI is therefore able to track the transition from US EPA Tier 2 standards (in 2006) through to Tier 4 (in 2012) to the present and in so doing demonstrate the efficacy of this policy. Furthermore, this analysis shows that had the fleet remained at Tier 1 (emission intensity) the surface mines would currenty be emitting an additional 40 kt[NO$_2$]/yr, or an additional 35% of the current total, an amount equivalent to that from a city of ∼5M inhabitants (Fioletov et al., 2022).

Some improvements over other studies include a more consistent, emissions-based scaling to convert NO_2 to NO_x, which was found to give a conversion factor about 10% larger than simple NO_x/NO_2 concentration ratio. Another improvement lay in the use of an evolving effective lifetime, reflecting the fact that NO_2 impacts its own loss rate. In addition to emissions, this work better connects the point source and area source emissions methods and discusses the interpretation of fitting parameters and the ability to resolve emissions from sources in close proximity.

Data availability. Original OMI Level 2, orbit-based NO_2 data are available from the NASA Goddard Earth Sciences Data and Information Services Center (https://aura.gesdisc.eosdis.nasa.gov/data/Aura_OMI_Level2/OMNO2.003/). ECMWF (European Centre for Medium-Range Weather Forecasts) reanalysis data (ERA5) are available here, https://www.ecmwf.int/en/forecasts/datasets/browse-reanalysis-datasets. The North-America-wide OMI NO_2 VCDs reprocessed using ECCC air mass factors used in this work are available at https://collaboration. cmc.ec.gc.ca/cmc/arqi/OilSands_satellite_NO2data in netcdf format.

Code and data availability. The analysis code was written in Matlab, and is available from the authors upon request.

Appendix A: The Oil Sands Surface Mining Facilities

The individual mining facilities are shown in Figure A1.

Appendix B: The Two-dimensional Exponentially-Modified Gaussian Plume Function

The two-dimensional exponentially-modified Gaussian (EMG) is used to model the vertical column density, VCD, distribution of the plume as seen from a satellite instrument. It is preferred over the traditional Gaussian plume (Stockie, 2011) as it better accounts for the finite spatial extent of the source itself, and the relatively coarse spatial resolution of the satellite observations being utilized. Mathematically it is the convolution of a two dimensional Gaussian (i.e., integrated through the vertical dimensional) and an exponential. It depends on the cross-wind distance, x, and the downwind distance, y, each in km and relative to the location of the emission source, and the wind speed, s, in km/hr and where the wind is aligned in the y-direction. Carrying out the convolution leads to the following functional form, described by equations B1-B5,

$$\mathrm{VCD}(x, y, s) = \mathrm{EMG}(x, y, s) = a \cdot f(x, y) \cdot g(y, s) \tag{B1}$$

where the function f and g are,

$$f(x, y) = \frac{1}{\sigma_1 \sqrt{2\pi}} \cdot \exp\left(-\frac{x^2}{2\sigma_1^2} \right) \tag{B2}$$

$$g(y, s) = \frac{\lambda_1}{2} \cdot \exp\left(\frac{\lambda_1(\lambda_1 \sigma^2 - 2y)}{2} \right) \cdot \mathrm{erfc}\left(\frac{\lambda_1 \sigma^2 - y}{\sqrt{2}\sigma} \right) \tag{B3}$$
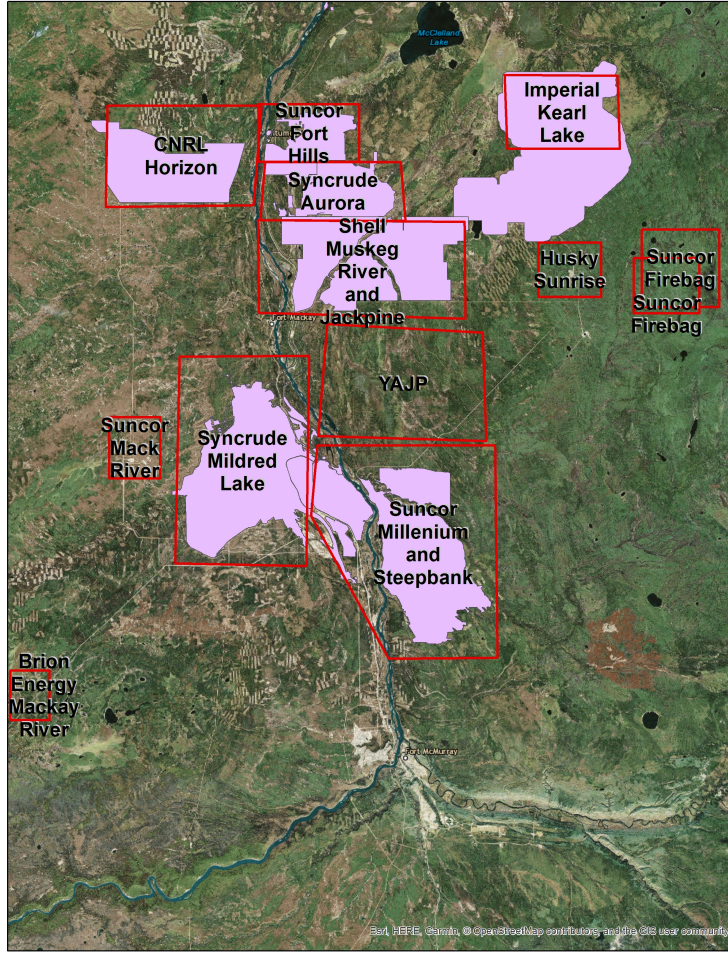
Figure A1. Location and name of all mining facilities.

and where

$$
\sigma_1 = \begin{cases} \sqrt{\sigma^2 + 1.5y} & , \; y > 0 \\ \sigma & , \; y \le 0 \end{cases}
\tag{B4}
$$

$$
\lambda_1 = \frac{1}{\tau \cdot s}.
\tag{B5}
$$

The a factor represents the concentration enhancement by the source and is directly proportional to the mass of the enhancement, m; σ is the parameter describing the width of the Gaussian [in km], τ is the effective lifetime (in hours) and $\mathrm{erfc}(x) = \frac{2}{\sqrt{\pi}} \int_x^\infty e^{-t^2} dt$. This formulation is the same as in Fioletov et al. (2015) except that y has been replaced by $-y$ so
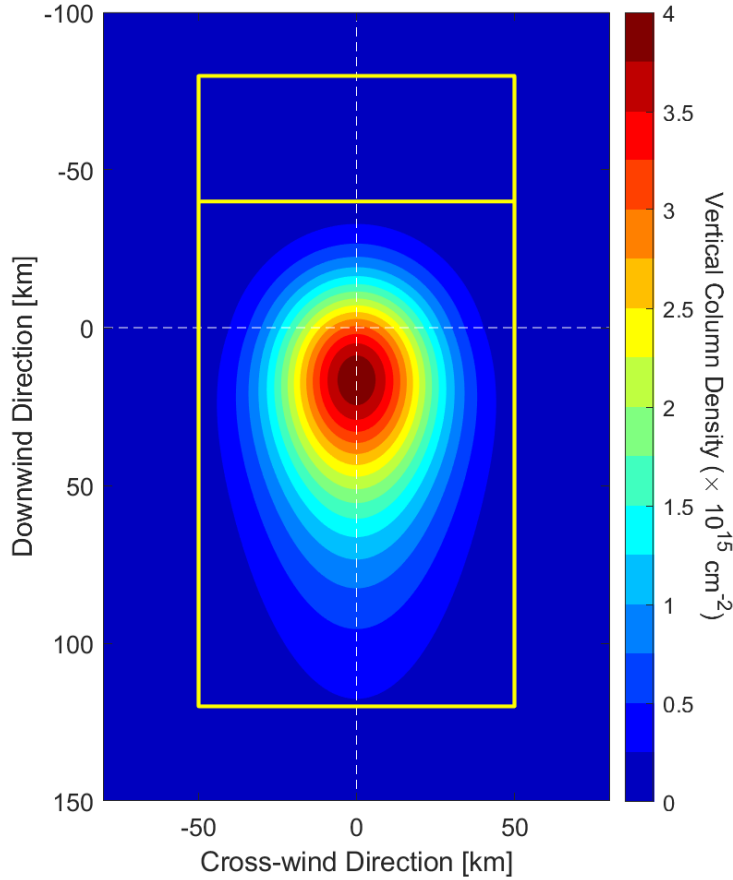
Figure B1. Sample of NO$_2$ VCDs generated using the EMG plume function as defined in equations B1–B5. In this example E=50 kt[NO$_2$]/yr, $\tau = 2.8$ hours, $\sigma = 18$ km and a constant wind speed of 12 km/hr was specified. The upper box shows the domain used to calculate the background, where the lower box shows the domain over with the EMG function is fit. The limits in x are ± 50 km and $y = -80$ to -40 km for the background, and $y = -40$ to 120 km for the fit. No background NO$_2$ was added in this example.

that distances downwind of the source are now positive. The emission rate is given by $E = m/\tau$, and ultimately the distribution is characterized by (E, τ, σ). See Fioletov et al. (2015) for additional information.

     Equation B2 can be recognized as the standard Gaussian describing the cross-wind distribution, and is a function of the downwind distance via the diffusion term embedded in σ_1. In equation B3, $g(y,s)$ is a convolution of a Gaussian and and exponential in the downwind direction, where the exponential accounts for first-order loss due to chemistry and deposition (with decay rate τ, and thus the decay being $\sim \exp[-y/(\tau \cdot s)]$, and $\lambda_1 = \lambda/s$ from equation B5).

Appendix C: Implementation of the Point Source Method

The point source method involves a non-linear fit of OMI VCDs to the EMG as detailed in appendix B. Here, the solution is obtained using the non-linear least-squares solver "lsqnonlin.m" in Matlab. The non-linear terms are the lifetime and width parameters, whereas the mass is a linear scaling of the EMG.

It is important to note that the reference location must be specified as part of the point source method, where the reference location is the location of the emission source. In the case of a somewhat extended, or pseudo-point source, the centre of the emission source(s) is used. Here, wind information comes from the ECMWF ERA-interim or ERA-5 reanalyses (Dee et al., 2011) interpolated in space and time to the location of each OMI pixel.

In order to combine many overpasses where wind direction is constantly changing, a wind rotation scheme is used (Pommier et al., 2013) where the location of the OMI pixel (as denoted by the pixel centre) is rotated about the reference location so that wind directions are aligned (see also Fioletov et al. (2015)).

Background levels of NO_2 must be accounted for when deriving NO_x emissions, where background in this context refers to the NO_2 that would be present if the source in question were removed. This can be done by additionally including a constant as part of the EMG fit, or, as here, an upwind average can be determined and subtracted from all VCDs before the fit. This is illustrated in Figure B1, which shows a sample EMG plume and the two domains used for the fit. The average over the upwind box (between $x = \pm 50$ and $y = -80$ to -40 km) is used to calculate the background, which accounts for any NO_2 not emitted locally, as well as potential offsets due to an imperfect stratospheric removal. The larger box is the domain over which the non-linear fit is performed ($x = \pm 40$ km and $y = -40$ to 120 km).

While the fitting is carried out in the rotated frame, the agreement with the orignal mean OMI VCD dsitribution can be assessed by taking the fitted EMG and rotating it back to the original co-ordinates. This is called the reconstruction, and it highlights one advantage of using this 2D approach where spatial information is not lost in an averaging.

Figure 2 shows the mean OMI VCD, OMI rotated VCD, fitted VCD, and reconstructed VCD plots considering all years of OMI data. Analogous plots are shown here but considering only a single 3-year period, 2005–2007, in Figure C1. Each three year period considered, even those in later years with reduced data, are comparable in fit quality. This time period was chosen as it predates much of the expansion of the northern mines, and thus better represents a point source as reflected by a smaller width parameter, $\sigma = 17.5$ km vs 20.6 km, and smaller total emissions, $E = 55$ vs 70 kt[NO_2)]yr, as compared to the all-year analysis.

Appendix D: Implementation of the Multi-source Method

To determine emissions from multiple sources, a related method has been developed (Fioletov et al., 2017; McLinden et al., 2020) whereby each (potential) source location is treated as an EMG plume. The total VCD is therefore the sum over all
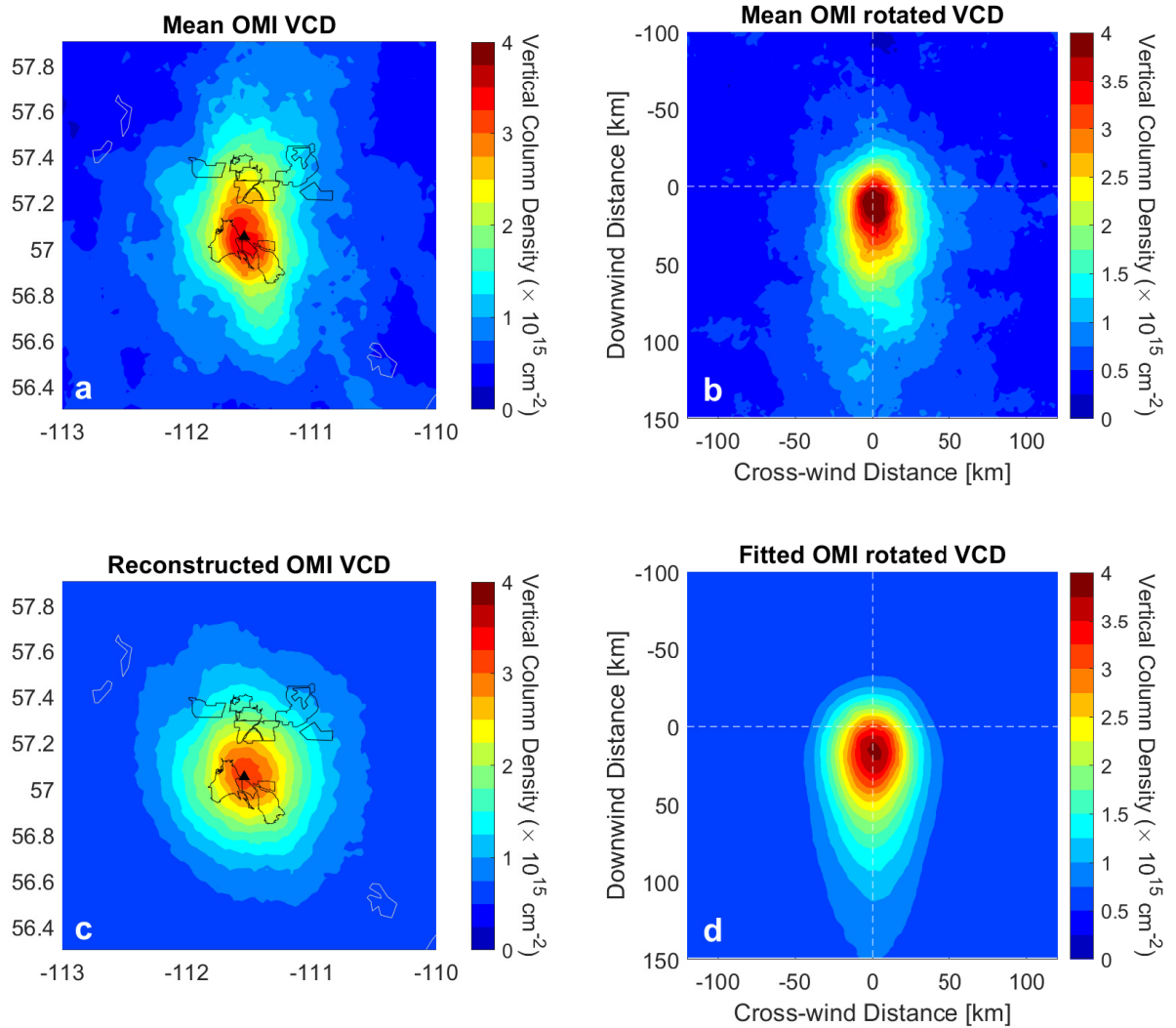
Figure C1. Summary of the point source emissions procedure using 2005–2007 OMI NO$_2$ VCDs. (a) Mean OMI VCD over the surface mining region of the oil sands. The black lines denote the different mining operations; (b) mean OMI VCD after rotation showing plume-like structure; (c) Reconstructed spatial distribution using EMG plume and fitted parameters; (d) Fit to rotated VCD using 2D EMG plume function, with fitted parameters of $E = 55.3$ kt[NO$_2$]/yr, $\tau = 2.8$ hours, and $\sigma = 17.6$ km. The black triangle in the panels (a) and (c) show the reference location used in the emissions retrieval and corresponds to the (0, 0) point in panels (b) and (d).

plumes, plus the background term(s),

$$\text{VCD}(x, y, s) = a_0 + \sum_{i=1}^{N} a_i \cdot \mathcal{R}\left[\text{EMG(x, y, s)}\right] \tag{D1}$$
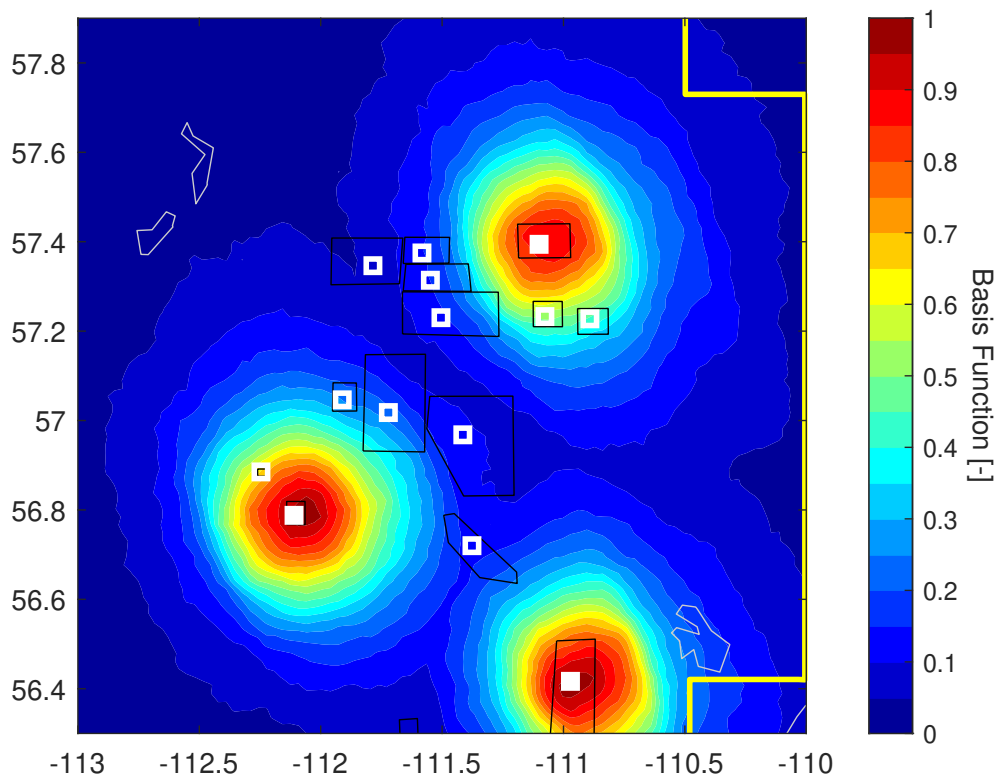
Figure D1. Examples of averaged OMI NO$_2$ multi-source fit basis functions. The black polygons outline the boundaries of the NO$_x$ source, and the white square are the locations where the emissions are allowed to emanate. For three locations, indicated by the filled squares, the average plume shape is shown. An averaging radius of 12 km was used.

600   where N is the total number of sources, and x, y, and s are as in A and are specific to each emissions. The downwind and cross-wind distances, y and x, will differ from location to location as these are distances, after rotation, between all pixels being considered and source i. Furthermore, there will be some modest variation in windspeed, s, as these are also location specific and derived from an interpolation of the ERA-5 (31 km, (Hersbach et al., 2020)) wind fields. The EMG function is also as above but here the $\mathcal{R}$ denotes that EMG was transformed, or rotated, back into the original latitude and longitude co-ordinates.

605   These rotated EMG functions then serve as basis functions in a system of linear equations in latitude-longitude space. The non-linear coefficients in the EMG Gaussian terms, f and g, equations (B2) and (B3), are specified and not fit. The matlab function lsqlin.m was used with a positive constraint placed on all values of the fitted a_i coefficients, which are linearly related to the emission rate. Here a constant, a_0, is also fitted and represents the background NO$_2$ that would be present in absence of these local sources. The constant can be replaced by a more complicated background term as has been done in other studies,

610   such as a plane or a series of polynomials (Fioletov et al., 2022; Wren et al., 2023). However, here a constant was found to be sufficient only a relatively small domain is being considered. In this work source locations were specified as either being on a grid or at the centre of each known source.

The idea behind the multi-source method is better illustrated using Figure D1. In this example, emissions are allowed to emanate (although the magnitude of the emissions may be zero) from 14 locations identified by the white squares, each of which corresponds to a known source of NO_x, either a surface mine, in-situ mine, or community, in the domain under consideration. For locations indicated by the filled squares, the average rotated EMG plume is shown. Here, only three of the potential emissions locations are shown for clarity, but in the fitting procedure, each square (open or filled) would have a similar looking distribution. The distribution associated with each location represents the average NO_2 VCD spatial pattern expected and are the basis function in the multi-linear fit. The slight elongation of the pattern reflects the fact that W and SW winds are the preferred wind direction. By fitting the OMI VCDs to equation (D1), a coefficient or scaling for each of these is determined that represents the emissions from that location. The sum over all sources, what is also called the reconstruction, should be in good agreement with the OMI distribution. Figures D3 can be compared with D2 to confirm the general consistency for all 3-year periods analyzed.

Appendix E: Emissions Calculations

Over the course of the OMI mission, a blockage known as the row-anomaly has meant a (generally) expanding number of pixels become unreliable, leading to a reduction in data density. It is for this reason that data are analyzed in three-year periods as opposed to 1 year. Figure E1a shows the impact of the row anomaly on observations within 80 km of the reference location (57.1°N, 111.6°W). Due to variations in solar zenith angle and cloud cover OMI does not sample evenly through the year. This variation is illustrated in Figure E1b, with each year generally following this same average pattern. There is uneven sampling throughout the year with little data in November- January due to low sun angles, and a drop in the summer due to increased cloud cover.

As a result of this uneven sampling, intra-annual changes in emissions may not be totally captured. To estimate this effect, monthly totals of bitumen mines (Alberta Energy Regulator, 2023a), which should be a good proxy for NO_x emissions, were examined. From Figure E2, monthly values fluctuate about the annual mean by roughly 10–15%.

A correction factor to account for this unequal sampling throughout the year was used. A monthly total bitumen-mined value was assigned to each OMI pixel (used in the emissions calculations), according to its month and year. For each year, the ratio of the mean monthly bitumen-mined to the average (over all OMI pixels) of the OMI-sampled bitumen-mined was computed. This ratio was found to vary from 1.00 to 1.05. It was then used to scale the retrieved emissions in Figures 9 and 10, and Table E1, below. These values are smaller than those derived for OMI SO_2 (McLinden et al., 2020) as coverage for NO_2 is less seasonally-dependent.

As discussed in section 2.4.3, the missing component of NO_x, NO, is accounted for using an externally-derived NO_2/NO_x ratio. Figure E3 shows a comparison of observed ratios made during the 2018 aircraft campaign in which plumes were tracked downwind of the surface mines. An evolution is observed from values around 0.6 to 0.75 due to photochemical processing. These observations can be compared to the emissions-based method of estimating NO_2/NO_x, which accounts for downwind effect, appropriate for annual and June-July time periods, with the latter done to be more consistent with the observations time

Table E1. Summary of emissions calculations employing algorithm variants. Emissions given here are averages over the entire 2005–2024 OMI period. Average NPRI stack emissions (2005–2023) are 30.5 kt[NO_2/yr]. The mean over all methods, and the variability among methods, is given in the bottom row.

Emission run	Algorithm	(τ, σ)	Gridded Emissions	Point Sources Specified	Wind height adjustment	OMI Emissions kt[NO_2/yr] Fleet	OMI Emissions kt[NO_2/yr] Total
TOTAL1	Point	Fitted	N/A	N/A	No	N/A	78.0
TOTAL2	Multi	Specified	Yes	No	No	N/A	74.0
TOTAL3	Multi	Specified	No	No	No	N/A	72.4
FLEET1	Multi	Specified	Yes	Yes	No	43.6	74.7
FLEET2	Multi	Specified	No	Yes	No	43.6	74.7
FLEET3	Multi	Specified	Yes	Yes	Yes	47.2	78.3
FLEET4	Multi	Specified	No	Yes	Yes	42.2	73.3
					Mean $\pm$ Standard Deviation	44.1 ± 2.1	75.1 ± 2.3

period. The good overall consistency suggests the emissions-based approach is reasonable. Further, an estimate of uncertainty is derived by looking at the variability.

Emissions calculations were carried out using the point source and several different variants of the multi source methods. The purpose was to test different assumptions as well as to conduct a sensitivity study that could be used to help quantify uncertainties. A summary is of the various emission runs is provided in Table E1.

Seven runs were used: the point source method, and six multi-source variants. Variables changed for the multi-source runs included: fitting all emissions using the gridded and mine-specific approach, fitting only fleet emissions (with point source emissions specified) using the gridded and mine-specific approach, and fitting only fleet emissions using the gridded and mine-specific approach but using higher altitude winds for the stack emissions and lower altitude winds for the fleet. As can be seen from Table E1 there is little difference among them.

Appendix F: Resolution and the width parameter, σ

The relationship between σ, σ_{diff}, σ_{size}, and σ_{pixel} was explored in appendix F using a simple model in which a collection of true-Gaussian plume point sources were used to simulate a near point source (of some radius σ_{size}) and smoothed to satellite resolution (for pixel size σ_{pixel}). Fitting the combined distribution to an EMG allowed a relationship between these various terms to be established. Figure F1 shows σ has has a behaviour reminiscent of σ_{size}^2 and $\sigma_{\mathrm{pixel}}^2$, and for small values of both, values less than 1 km which suggests σ_{diff} is small. Figure F1 will be used below to help interpret results.

The behaviour of the fitted width parameter, σ, is further examined here in an attempt to understand how it varies with the spatial size or extent of the source, σ_{size}, satellite pixel size, σ_{pixel}, and the plume diffusion term, σ_{diff}. To do this, a set of numerical experiments were performed in which a collection of true-Gaussian plume point sources were used to simulate a

near point source (of some radius σ_{size}) and smoothed to satellite resolution (for pixel size σ_{pixel}). The Gaussian plume is of the form given in Stockie (2011) (with $\alpha = 0.33$ km, $\beta = 0.86$) but integrated in the vertical to simulate VCDs. Each Gaussian was sampled at high spatial resolution, 0.1 km, and the composite distribution was calculated by summing over all Gaussian plumes. This was smoothed to coarser resolutions in order to simulate observations from satellite instruments.

An EMG was then fit to the resultant distribution in order to derive σ. By varying σ_{size} and σ_{pixel}, Figure F1 is derived, which shows a behaviour consistent with equation 1. For the smallest case explored, $\sigma_{\mathrm{size}} = 0.1$ km and $\sigma_{\mathrm{pixel}} = 0.4$ km, a σ of 0.35 km was found. This can be interpreted as representing the diffusion term and confirms, at least for the EMG formulation, that it is small on this scale. Given this, the form,

$$\sigma^2 = a + b \cdot \sigma_{\mathrm{pixel}}^2 + c \cdot \sigma_{\mathrm{size}}^2, \tag{F1}$$

with $a = 0.33$ km^2, $b = 0.41$, and $c = 0.28$, is a good representation for the domain considered here. Interestingly, as σ_{pixel} was defined as a length of a square and σ_{size} as a radius, their weights are roughly equal when area is considered.

According to Figure F1 and with the effective pixel size of OMI (as defined as the square root of the average pixel area) being about 20 km, a σ of 15 km is expected. From section 3.2, OMI views a point source with $\sigma = 11$ km, a value close but slightly smaller than the 13 km from this numerical experiment. The difference could be related to the fact OMI pixels are not square (as assumed here) and also there is a considerable amount of oversampling by using multiple years of observations.

In the context of this multi-source method, an estimate of the minimum separation distance required to resolve between neighbouring emissions can be estimated by considering their basis functions. The criteria adopted here is that emissions from neighbouring sources can found as long as the correlation between their basis functions does not exceed 0.5. Using this, the minimum distance between sources as a function of lifetime, τ, and width parameter, σ, is shown in Figure F2. For OMI, this suggests sources $\sim$22 km apart can be resolved. If a more relaxed threshold of 0.7 is used then this decreases to about 15.5 km. Wind is also important: if the winds are halved there is less overlap of the plumes, and 20 km is required; likewise, doubling the wind speed increases this to 24 km. Note that while this suggests low wind speeds are advantageous, in reality this also means the plumes are not as evident making an accurate emissions calculation more difficult.

TROPOMI, with its significantly improved spatial resolution relative to OMI (a 12-fold improvement in area, or 3–4 fold improvement in distance), will mean much smaller values for σ, and hence an improved ability to resolve emissions.

Even though emissions from the multi-source method were simply summed to a total over all surface mining based on a minimum separation distance of OMI of about 22 km, it is nonetheless worth attempt to resolve them. Here we consider the approach in which one source is assigned to each mine (e.g., see Figure 8) and consider the period 2010–2020 where reported emissions are available for both stack and fleet sources. A scatterplot of the facility-specific emissions is shown in Figure F3

For distances between mines of less than about 12 km, with one exception, OMI has difficulty distinguishing between neighbouring sources and can misassign emissions. The two larger emission sources, Syncrude-Mildred Lake and Suncor, each with reported emissions of about 20 kt[NO$_2$]/yr, are resolved fairly well. Even though Suncor is only about 7 km from its nearest neighbour, it also emits an order of magnitude more NO$_x$. Overall OMI does show some limited ability to resolve

emissions between neighbouring mines. This may suggest that a correlation threshold of 0.5 is too stringent, and that perhaps a value of 0.7, which leads to a minimum separation distance of 17 km, is more reasonable.

Author contributions. CM wrote the paper and performed the analysis. VF, CM, DG, and ED developed the methodology. JZ and CA provided emissions and proxy-data . NK and LL provided the OMI data. All co-authors provided comments and feedback to CM.

Competing interests. There are not competing interests.

Acknowledgements. The authors would like to thank the Wood Buffalo Environmental Association (WBEA) for the provision of their in situ data. We acknowledge the NASA Earth Science Division for funding of OMI NO_2 product development and analysis, and the Air Quality Research Division support teams and the National Research Council aircraft pilots and technical support team for the aircraft measurement campaign. The aircraft measurement campaign projects were funded by the Oil Sands Monitoring (OSM) program by the Governments of Alberta and Canada. The authors also thank Richard Melick from the Government of Alberta for providing the off-road fleet NO_x emissions data.

References

710 Adams, C., McLinden, C., Shephard, M., Dickson, N., Dammers, E., Chen, J., Makar, P., Cady-Pereira, K., Tam, N., Kharol, S., Lamsal, L., and Krotkov, N.: Satellite-derived emissions of carbon monoxide, ammonia, and nitrogen dioxide from the 2016 Horse River wildfire in the Fort McMurray area, Atmospheric Chemistry and Physics, 19, 2577–2599, https://doi.org/10.5194/acp-19-2577-2019, https://www.atmos-chem-phys.net/19/2577/2019/acp-19-2577-2019.html, cited By 4, 2019.

Alberta Energy Regulator: ST39: Alberta Mineable Oil Sands Plant Statistics Monthly Supplement, https://www.aer.ca/
715 providing-information/data-and-reports/statistical-reports/st39, accessed = 2024-08-20, 2023a.

Alberta Energy Regulator: ST98: Alberta Energy Outlook, https://www.aer.ca/providing-information/data-and-reports/statistical-reports/st98, last Accessed on 2024-08-20, 2023b.

Alberta Environment and Parks: Compilation of 2010-2023 oil sands mine fleet NOx emissions data from submitted industrial EPEA Approval Annual Air Reports, provided to Environment and Climate Change Canada, 2025.

720 Alberta Government: Continuous Emission Monitoring System (CEMS) Code, https://open.alberta.ca/publications/0773250387, 1998.

Beirle, S., Boersma, K. F., Platt, U., Lawrence, M. G., and Wagner, T.: Megacity Emissions and Lifetimes of Nitrogen Oxides Probed from Space, Science, 333, 1737–1739, https://doi.org/10.1126/science.1207824, http://science.sciencemag.org/content/333/6050/1737, 2011.

Beirle, S., Borger, C., Dörner, S., Li, A., Hu, Z., Liu, F., Wang, Y., and Wagner, T.: Pinpointing nitrogen oxide emissions from space, Science Advances, 5, https://doi.org/10.1126/sciadv.aax9800, https://advances.sciencemag.org/content/5/11/eaax9800, 2019.

725 Boersma, K. F., Eskes, H. J., Dirksen, R. J., van der A, R. J., Veefkind, J. P., Stammes, P., Huijnen, V., Kleipool, Q. L., Sneep, M., Claas, J., Leitão, J., Richter, A., Zhou, Y., and Brunner, D.: An improved tropospheric NO$_2$ column retrieval algorithm for the Ozone Monitoring Instrument, Atmos. Meas. Tech., 4, 1905, 2011.

Cooper, M. J., Martin, R. V., Lyapustin, A. I., and McLinden, C. A.: Assessing snow extent data sets over North America to inform and improve trace gas retrievals from solar backscatter, Atmospheric Measurement Techniques, 11, 2983–2994, https://doi.org/10.5194/amt-
730 11-2983-2018, https://www.atmos-meas-tech.net/11/2983/2018/, 2018.

Dammers, E., McLinden, C. A., Griffin, D., Shephard, M. W., Van Der Graaf, S., Lutsch, E., Schaap, M., Gainairu-Matz, Y., Fioletov, V., Van Damme, M., Whitburn, S., Clarisse, L., Cady-Pereira, K., Clerbaux, C., Coheur, P. F., and Erisman, J. W.: NH$_3$ emissions from large point sources derived from CrIS and IASI satellite observations, Atmospheric Chemistry and Physics, 19, 12 261–12 293, https://doi.org/10.5194/acp-19-12261-2019, https://www.atmos-chem-phys.net/19/12261/2019/, 2019.

735 de Foy, B., Wilkins, J. L., Lu, Z., Streets, D. G., and Duncan, B. N.: Model evaluation of methods for estimating surface emissions and chemical lifetimes from satellite data, Atmospheric Environment, 98, 66 – 77, https://doi.org/https://doi.org/10.1016/j.atmosenv.2014.08.051, http://www.sciencedirect.com/science/article/pii/S1352231014006530, 2014.

de Foy, B., Lu, Z., Streets, D. G., Lamsal, L. N., and Duncan, B. N.: Estimates of power plant NO$_x$ emissions and lifetimes from OMI NO$_2$ satellite retrievals, Atmospheric Environment, 116, 1 – 11, https://doi.org/https://doi.org/10.1016/j.atmosenv.2015.05.056, http://www.
740 sciencedirect.com/science/article/pii/S1352231015301291, 2015.

Dee, D. P., Uppala, S. M., Simmons, A. J., Berrisford, P., Poli, P., Kobayashi, S., Andrae, U., Balmaseda, M. A., Balsamo, G., Bauer, P., Bechtold, P., Beljaars, A. C. M., van de Berg, L., Bidlot, J., Bormann, N., Delsol, C., Dragani, R., Fuentes, M., Geer, A. J., Haimberger, L., Healy, S. B., Hersbach, H., Hólm, E. V., Isaksen, L., Kållberg, P., Köhler, M., Matricardi, M., McNally, A. P., Monge-Sanz, B. M., Morcrette, J.-J., Park, B.-K., Peubey, C., de Rosnay, P., Tavolato, C., Thépaut, J.-N., and Vitart, F.: The ERA-Interim reanalysis:

745   configuration and performance of the data assimilation system, Quarterly Journal of the Royal Meteorological Society, 137, 553–597, https://doi.org/10.1002/qj.828, http://dx.doi.org/10.1002/qj.828, 2011.

Environment and Climate Change Canada: National Pollutant Release Inventory, https://www.canada.ca/en/services/environment/pollution-waste-management/national-pollutant-release-inventory.html, last Accessed on 2020-01-20, 2020.

Environment Protection Agency: EPA-420-B-16-02: Nonroad Compression-Ignition Engines: Exhaust Emission Standards, https://nepis.
750   epa.gov/Exe/ZyPDF.cgi?Dockey=P100OA05.pdf, accessed = 2021-08-20, 2016.

Fioletov, V., McLinden, C. A., Kharol, S. K., Krotkov, N. A., Li, C., Joiner, J., Moran, M. D., Vet, R., Visschedijk, A. J. H., and Denier van der Gon, H. A. C.: Multi-source SO_2 emission retrievals and consistency of satellite and surface measurements with reported emissions, Atmospheric Chemistry and Physics, 17, 12 597–12 616, https://doi.org/10.5194/acp-17-12597-2017, https://www.atmos-chem-phys.net/17/12597/2017/, 2017.

755   Fioletov, V., McLinden, C. A., Griffin, D., Krotkov, N., Liu, F., and Eskes, H.: Quantifying urban, industrial, and background changes in NO_2 during the COVID-19 lockdown period based on TROPOMI satellite observations, Atmospheric Chemistry and Physics, 22, 4201–4236, https://doi.org/10.5194/acp-22-4201-2022, https://acp.copernicus.org/articles/22/4201/2022/, 2022.

Fioletov, V., McLinden, C. A., Griffin, D., Zhao, X., and Eskes, H.: Global seasonal urban, industrial, and background NO_2 estimated from TROPOMI satellite observations, Atmospheric Chemistry and Physics, 25, 575–596, https://doi.org/10.5194/acp-25-575-2025, https:
760   //acp.copernicus.org/articles/25/575/2025/, 2025.

Fioletov, V. E., McLinden, C. A., Krotkov, N., Moran, M. D., and Yang, K.: Estimation of SO_2 emissions using OMI retrievals, Geophysical Research Letters, 38, https://doi.org/10.1029/2011GL049402, https://agupubs.onlinelibrary.wiley.com/doi/abs/10.1029/2011GL049402, 2011.

Fioletov, V. E., McLinden, C. A., Krotkov, N., and Li, C.: Lifetimes and emissions of SO_2 from point sources estimated from OMI, Geophysi-
765   cal Research Letters, 42, 1969–1976, https://doi.org/10.1002/2015GL063148, http://dx.doi.org/10.1002/2015GL063148, 2015GL063148, 2015.

Fioletov, V. E., McLinden, C. A., Krotkov, N., Li, C., Joiner, J., Theys, N., Carn, S., and Moran, M. D.: A global catalogue of large SO_2 sources and emissions derived from the Ozone Monitoring Instrument, Atmospheric Chemistry and Physics, 16, 11 497–11 519, https://doi.org/10.5194/acp-16-11497-2016, https://www.atmos-chem-phys.net/16/11497/2016/, 2016.

770   Galarneau, E., Hollebone, B., Yang, Z., and Schuster, J.: Preliminary measurement-based estimates of PAH emissions from oil sands tailings ponds, Atmospheric Environment, 97, 332–335, https://doi.org/10.1016/j.atmosenv.2014.08.038, https://www.scopus.com/inward/record.uri?eid=2-s2.0-84906350939&doi=10.1016%2fj.atmosenv.2014.08.038&partnerID=40&md5=62673ccccd8336620eb95b23a7e110ef, cited By 33, 2014.

Goldberg, D. L., Lu, Z., Oda, T., Lamsal, L. N., Liu, F., Griffin, D., McLinden, C. A., Krotkov, N. A., Duncan, B. N., and Streets,
775   D. G.: Exploiting OMI NO_2 satellite observations to infer fossil-fuel CO_2 emissions from U.S. megacities, Science of The Total Environment, 695, 133 805, https://doi.org/https://doi.org/10.1016/j.scitotenv.2019.133805, https://www.sciencedirect.com/science/article/pii/S0048969719337465, 2019a.

Goldberg, D. L., Lu, Z., Streets, D. G., de Foy, B., Griffin, D., McLinden, C. A., Lamsal, L. N., Krotkov, N. A., and Eskes, H.: Enhanced Capabilities of TROPOMI NO2: Estimating NOX from North American Cities and Power Plants, Environmental Science & Technology,
780   53, 12 594–12 601, https://doi.org/10.1021/acs.est.9b04488, https://doi.org/10.1021/acs.est.9b04488, pMID: 31601103, 2019b.

Gordon, M., Li, S.-M., Staebler, R., Darlington, A., Hayden, K., O'Brien, J., and Wolde, M.: Determining air pollutant emission rates based on mass balance using airborne measurement data over the Alberta oil sands operations, Atmospheric Measurement Techniques, 8, 3745–3765, https://doi.org/10.5194/amt-8-3745-2015, https://www.atmos-meas-tech.net/8/3745/2015/, 2015.

Griffin, D., McLinden, C. A., Dammers, E., Adams, C., Stockwell, C. E., Warneke, C., Bourgeois, I., Peischl, J., Ryerson, T. B., Zarzana, K. J., Rowe, J. P., Volkamer, R., Knote, C., Kille, N., Koenig, T. K., Lee, C. F., Rollins, D., Rickly, P. S., Chen, J., Fehr, L., Bourassa, A., Degenstein, D., Hayden, K., Mihele, C., Wren, S. N., Liggio, J., Akingunola, A., and Makar, P.: Biomass burning nitrogen dioxide emissions derived from space with TROPOMI: methodology and validation, Atmospheric Measurement Techniques, 14, 7929–7957, https://doi.org/10.5194/amt-14-7929-2021, https://amt.copernicus.org/articles/14/7929/2021/, 2021.

Helfrich, S. R., McNamara, D., Ramsay, B. H., Baldwin, T., and Kasheta, T.: Enhancements to, and forthcoming developments in the Interactive Multisensor Snow and Ice Mapping System (IMS), Hydrological Processes, 21, 1576–1586, https://doi.org/10.1002/hyp.6720, https://onlinelibrary.wiley.com/doi/abs/10.1002/hyp.6720, 2007.

Hersbach, H., Bell, B., Berrisford, P., Hirahara, S., Horányi, A., Muñoz-Sabater, J., Nicolas, J., Peubey, C., Radu, R., Schepers, D., Simmons, A., Soci, C., Abdalla, S., Abellan, X., Balsamo, G., Bechtold, P., Biavati, G., Bidlot, J., Bonavita, M., De Chiara, G., Dahlgren, P., Dee, D., Diamantakis, M., Dragani, R., Flemming, J., Forbes, R., Fuentes, M., Geer, A., Haimberger, L., Healy, S., Hogan, R. J., Hólm, E., Janisková, M., Keeley, S., Laloyaux, P., Lopez, P., Lupu, C., Radnoti, G., de Rosnay, P., Rozum, I., Vamborg, F., Villaume, S., and Thépaut, J.-N.: The ERA5 global reanalysis, Quarterly Journal of the Royal Meteorological Society, 146, 1999–2049, https://doi.org/https://doi.org/10.1002/qj.3803, https://rmets.onlinelibrary.wiley.com/doi/abs/10.1002/qj.3803, 2020.

Ialongo, I., Fioletov, V., McLinden, C., Jåfs, M., Krotkov, N., Li, C., and Tamminen, J.: Application of satellite-based sulfur dioxide observations to support the cleantech sector: Detecting emission reduction from copper smelters, Environmental Technology and Innovation, 12, 172–179, https://doi.org/10.1016/j.eti.2018.08.006, https://www.scopus.com/inward/record.uri?eid=2-s2.0-85053782807&doi=10.1016%2fj.eti.2018.08.006&partnerID=40&md5=03394869c5ae818cf12ef210cf081fb3, cited By 3, 2018.

Kelly, E. N., Schindler, D. W., Hodson, P. V., Short, J. W., Radmanovich, R., and Nielsen, C. C.: Oil sands development contributes elements toxic at low concentrations to the Athabasca River and its tributaries, Proceedings of the National Academy of Sciences, 107, 16178–16183, https://doi.org/10.1073/pnas.1008754107, https://www.pnas.org/content/107/37/16178, 2010.

Krol, M., van Stratum, B., Anglou, I., and Boersma, K. F.: Evaluating NO_x stack plume emissions using a high-resolution atmospheric chemistry model and satellite-derived NO_2 columns, Atmospheric Chemistry and Physics, 24, 8243–8262, https://doi.org/10.5194/acp-24-8243-2024, https://acp.copernicus.org/articles/24/8243/2024/, 2024.

Krotkov, N. A., Lamsal, L. N., Marchenko, S. V., Celarier, E. A., J.Bucsela, E., Swartz, W. H., and Veefkind, P.: OMI/Aura Nitrogen Dioxide (NO_2) Total and Tropospheric Column 1-orbit L2 Swath 13x24 km V003, https://doi.org/10.5067/Aura/OMI/DATA2017, accessed: February 21, 2019, 2018.

Lamsal, L. N., Krotkov, N. A., Vasilkov, A., Marchenko, S., Qin, W., Yang, E.-S., Fasnacht, Z., Joiner, J., Choi, S., Haffner, D., Swartz, W. H., Fisher, B., and Bucsela, E.: Ozone Monitoring Instrument (OMI) Aura nitrogen dioxide standard product version 4.0 with improved surface and cloud treatments, Atmospheric Measurement Techniques, 14, 455–479, https://doi.org/10.5194/amt-14-455-2021, https://amt.copernicus.org/articles/14/455/2021/, 2021.

Lange, K., Richter, A., and Burrows, J. P.: Variability of nitrogen oxide emission fluxes and lifetimes estimated from Sentinel-5P TROPOMI observations, Atmospheric Chemistry and Physics Discussions, 2021, 1–32, https://doi.org/10.5194/acp-2021-273, https://acp.copernicus.org/preprints/acp-2021-273/, 2021.

Laughner, J. L. and Cohen, R. C.: Direct observation of changing NOx lifetime in North American cities, Science, 366, 723–727, https://doi.org/10.1126/science.aax6832, https://science.sciencemag.org/content/366/6466/723, 2019.

820 Levelt, P. F., van den Oord, G. H. J., Dobber, M. R., Mälkki, A., Visser, H., de Vries, J., Stammes, P., Lundell, J. O. V., and Saari, H.: The Ozone Monitoring Instrument, IEEE Trans. Geosci. Remote Sens., 44, 1093, 2006.

Levelt, P. F., Joiner, J., Tamminen, J., Veefkind, J. P., Bhartia, P. K., Stein Zweers, D. C., Duncan, B. N., Streets, D. G., Eskes, H., van der A, R., McLinden, C., Fioletov, V., Carn, S., de Laat, J., DeLand, M., Marchenko, S., McPeters, R., Ziemke, J., Fu, D., Liu, X., Pickering, K., Apituley, A., González Abad, G., Arola, A., Boersma, F., Chan Miller, C., Chance, K., de Graaf, M., Hakkarainen, J., Hassinen, S.,

825 Ialongo, I., Kleipool, Q., Krotkov, N., Li, C., Lamsal, L., Newman, P., Nowlan, C., Suleiman, R., Tilstra, L. G., Torres, O., Wang, H., and Wargan, K.: The Ozone Monitoring Instrument: overview of 14 years in space, Atmospheric Chemistry and Physics, 18, 5699–5745, https://doi.org/10.5194/acp-18-5699-2018, https://www.atmos-chem-phys.net/18/5699/2018/, 2018.

Li, S.-M., Leithead, A., Moussa, S., Liggio, J., Moran, M., Wang, D., Hayden, K., Darlington, A., Gordon, M., Staebler, R., Makar, P., Stroud, C., McLaren, R., Liu, P., O'Brien, J., Mittermeier, R., Zhang, J., Marson, G., Cober, S., Wolde,

830 M., and Wentzell, J.: Differences between measured and reported volatile organic compound emissions from oil sands facil- ities in Alberta, Canada, Proceedings of the National Academy of Sciences of the United States of America, 114, E3756– E3765, https://doi.org/10.1073/pnas.1617862114, https://www.scopus.com/inward/record.uri?eid=2-s2.0-85019112086&doi=10.1073% 2fpnas.1617862114&partnerID=40&md5=7d5c5f9caf8d90d4e6fbb3f7d3d89f92, cited By 33, 2017.

Liggio, J., Li, S.-M., Hayden, K., Taha, Y., Stroud, C., Darlington, A., Drollette, B., Gordon, M., Lee, P., Liu, P., Leithead,

835 A., Moussa, S., Wang, D., O'Brien, J., Mittermeier, R., Brook, J., Lu, G., Staebler, R., Han, Y., Tokarek, T., Osthoff, H., Makar, P., Zhang, J., Plata, D., and Gentner, D.: Oil sands operations as a large source of secondary organic aerosols, Nature, 534, 91–94, https://doi.org/10.1038/nature17646, https://www.scopus.com/inward/record.uri?eid=2-s2.0-84973527082&doi=10.1038% 2fnature17646&partnerID=40&md5=dc931917c37bd123f4cf22df197b25ac, cited By 55, 2016.

Liggio, J., Li, S.-M., Staebler, R., Hayden, K., Darlington, A., Mittermeier, R., O'Brien, J., McLaren, R., Wolde, M., Worthy, D., and

840 Vogel, F.: Measured Canadian oil sands CO <inf>2</inf> emissions are higher than estimates made using internationally recom- mended methods, Nature Communications, 10, https://doi.org/10.1038/s41467-019-09714-9, https://www.scopus.com/inward/record.uri? eid=2-s2.0-85064926060&doi=10.1038%2fs41467-019-09714-9&partnerID=40&md5=60cac3392d96c199a65de9328276c4af, cited By 2, 2019.

Liu, M., van der A, R., van Weele, M., Eskes, H., Lu, X., Veefkind, P., de Laat, J., Kong, H., Wang, J., Sun, J., Ding, J., Zhao, Y., and Weng,

845 H.: A New Divergence Method to Quantify Methane Emissions Using Observations of Sentinel-5P TROPOMI, Geophysical Research Letters, 48, e2021GL094 151, https://doi.org/https://doi.org/10.1029/2021GL094151, https://agupubs.onlinelibrary.wiley.com/doi/abs/10. 1029/2021GL094151, e2021GL094151 2021GL094151, 2021.

Lorente, A., Folkert Boersma, K., Yu, H., Dörner, S., Hilboll, A., Richter, A., Liu, M., Lamsal, L. N., Barkley, M., De Smedt, I., Van Roozen- dael, M., Wang, Y., Wagner, T., Beirle, S., Lin, J.-T., Krotkov, N., Stammes, P., Wang, P., Eskes, H. J., and Krol, M.: Structural un-

850 certainty in air mass factor calculation for NO$_2$ and HCHO satellite retrievals, Atmospheric Measurement Techniques, 10, 759–782, https://doi.org/10.5194/amt-10-759-2017, https://www.atmos-meas-tech.net/10/759/2017/, 2017.

Makar, P. A., Staebler, R. M., Akingunola, A., Zhang, J., McLinden, C., Kharol, S. K., Pabla, B., Cheung, P., and Zheng, Q.: The effects of forest canopy shading and turbulence on boundary layer ozone, Nature Communications, 8, https://doi.org/10.1038/ncomms15243, 2017.

Makar, P. A., Akingunola, A., Aherne, J., Cole, A. S., Aklilu, Y.-A., Zhang, J., Wong, I., Hayden, K., Li, S.-M., Kirk, J., Scott, K.,

855 Moran, M. D., Robichaud, A., Cathcart, H., Baratzedah, P., Pabla, B., Cheung, P., Zheng, Q., and Jeffries, D. S.: Estimates of ex-

ceedances of critical loads for acidifying deposition in Alberta and Saskatchewan, Atmospheric Chemistry and Physics, 18, 9897–9927, https://doi.org/10.5194/acp-18-9897-2018, https://www.atmos-chem-phys.net/18/9897/2018/, 2018.

Martin, R., Jacob, D., Chance, K., Kurosu, T., Palmer, P., and Evans, M.: Global inventory of nitrogen oxide emissions constrained by space-based observations of NO2 columns, J. Geophys. Res., 108, cited By 3, 2003.

860 McLinden, C. A., Fioletov, V., Boersma, K. F., Krotkov, N., Sioris, C. E., Veefkind, J. P., and Yang, K.: Air quality over the Canadian oil sands: A first assessment using satellite observations, Geophysical Research Letters, 39, https://doi.org/10.1029/2011GL050273, https://agupubs.onlinelibrary.wiley.com/doi/abs/10.1029/2011GL050273, 2012.

McLinden, C. A., Fioletov, V., Boersma, K. F., Kharol, S. K., Krotkov, N., Lamsal, L., Makar, P. A., Martin, R. V., Veefkind, J. P., and Yang, K.: Improved satellite retrievals of NO_2 and SO_2 over the Canadian oil sands and comparisons with surface measurements, Atmospheric
865 Chemistry and Physics, 14, 3637–3656, https://doi.org/10.5194/acp-14-3637-2014, https://www.atmos-chem-phys.net/14/3637/2014/, 2014.

McLinden, C. A., Fioletov, V., Krotkov, N. A., Li, C., Boersma, K. F., and Adams, C.: A Decade of Change in NO_2 and SO_2 over the Canadian Oil Sands As Seen from Space, Environmental Science & Technology, 50, 331–337, https://doi.org/10.1021/acs.est.5b04985, http://dx.doi.org/10.1021/acs.est.5b04985, 2016a.

870 McLinden, C. A., Fioletov, V., Shephard, M. W., Krotkov, N., Li, C., Martin, R. V., Moran, M. D., and Joiner, J.: Space-based detection of missing sulfur dioxide sources of global air pollution, Nature-Geoscience, https://doi.org/10.1038/ngeo2724, 2016b.

McLinden, C. A., Adams, C. L. F., Fioletov, V., Griffin, D., Makar, P. A., Zhao, X., Kovachik, A., Dickson, N., Brown, C., Krotkov, N., Li, C., Theys, N., Hedelt, P., and Loyola, D. G.: Inconsistencies in sulfur dioxide emissions from the Canadian oil sands and potential implications, Environmental Research Letters, 16, 014 012, https://doi.org/10.1088/1748-9326/abcbbb, https://doi.org/10.1088/1748-9326/abcbbb,
875 2020.

M.J. Bradley & Associates: Evaluation of Vehicle Emissions Reduction Options for the Oil Sands Mining Fleet, p. 40, https://www.mjbradley.com/sites/default/files/Oil%20Sands%20Retrofit%20Feasibility%20Study%20Mar08_0.pdf, 2008.

MNP (Meyers Norris Penny): A Review of the 2016 Horse River Wildfire: Alberta Agriculture and Forestry Preparedness and Response, https://www.alberta.ca/assets/documents/Wildfire-MNP-Report.pdf, 2017.

880 Moran, M. D., Ménard, S., Talbot, D., Huang, P., Makar, P. A., Gong, W., Landry, H., Gravel, S., Gong, S., Crevier, L.-P., Kallaur, A., and Sassi, M.: Particulate-matter forecasting with GEM-MACH15, a new Canadian air-quality forecast model, in: Air Pollution Modelling and Its Application XX, Springer, Dordrecht, the Netherlands, 2010.

Nassar, R., Hill, T. G., McLinden, C. A., Wunch, D., Jones, D. B. A., and Crisp, D.: Quantifying CO_2 Emissions From Individual Power Plants From Space, Geophysical Research Letters, 44, 10,045–10,053, https://doi.org/10.1002/2017GL074702, http://dx.doi.org/10.1002/
885 2017GL074702, 2017GL074702, 2017.

Palmer, P. I., Jacob, D. J., Chance, K., Martin, R. V., Spurr, R. J. D., Kurosu, T. P., Bey, I., Yantosca, R., Fiore, A., and Li, Q.: Air mass factor formulation for spectroscopic measurements from satellites: Application to formaldehyde retrievals from the Global Ozone Monitoring Experiment, Journal of Geophysical Research: Atmospheres, 106, 14 539–14 550, https://doi.org/10.1029/2000JD900772, https://agupubs.onlinelibrary.wiley.com/doi/abs/10.1029/2000JD900772, 2001.

890 Pavlovic, R., Chen, J., Anderson, K., Moran, M. D., Beaulieu, P.-A., Davignon, D., and Cousineau, S.: The FireWork air quality forecast system with near-real-time biomass burning emissions: Recent developments and evaluation of performance for the 2015 North American wildfire season, Journal of the Air & Waste Management Association, 66, 819–841, https://doi.org/10.1080/10962247.2016.1158214, https://doi.org/10.1080/10962247.2016.1158214, pMID: 26934496, 2016.

Pendlebury, D., Gravel, S., Moran, M. D., and Lupu, A.: Impact of chemical lateral boundary conditions in a regional air quality forecast model on surface ozone predictions during stratospheric intrusions, Atmospheric Environment, 174, 148 – 170, https://doi.org/https://doi.org/10.1016/j.atmosenv.2017.10.052, http://www.sciencedirect.com/science/article/pii/S1352231017307185, 2018.

Pommier, M., McLinden, C. A., and Deeter, M.: Relative changes in CO emissions over megacities based on observations from space, Geophysical Research Letters, 40, 3766–3771, https://doi.org/10.1002/grl.50704, https://agupubs.onlinelibrary.wiley.com/doi/abs/10.1002/grl.50704, 2013.

Rosa, L., Davis, K. F., Rulli, M. C., and D'Odorico, P.: Environmental consequences of oil production from oil sands, Earth's Future, 5, 158–170, https://doi.org/10.1002/2016EF000484, https://agupubs.onlinelibrary.wiley.com/doi/abs/10.1002/2016EF000484, 2017.

Schaaf, C. B., Gao, F., Strahler, A. H., Lucht, W., Li, X., Tsang, T., Strugnell, N. C., Zhang, X., Jin, Y., Muller, J.-P., Lewis, P., Barnsley, M., Hobson, P., Disney, M., Roberts, G., Dunderdale, M., Doll, C., d'Entremont, R. P., Hu, B., Liang, S., Privette, J. L., and Roy, D.: First operational BRDF, albedo nadir reflectance products from MODIS, Remote Sensing of Environment, 83, 135 – 148, https://doi.org/https://doi.org/10.1016/S0034-4257(02)00091-3, http://www.sciencedirect.com/science/article/pii/S0034425702000913, the Moderate Resolution Imaging Spectroradiometer (MODIS): a new generation of Land Surface Monitoring, 2002.

Stockie, J. M.: The Mathematics of Atmospheric Dispersion Modeling, SIAM Review, 53, 349–372, https://doi.org/10.1137/10080991X, https://doi.org/10.1137/10080991X, 2011.

Streets, D. G., Canty, T., Carmichael, G. R., de Foy, B., Dickerson, R. R., Duncan, B. N., Edwards, D. P., Haynes, J. A., Henze, D. K., Houyoux, M. R., Jacob, D. J., Krotkov, N. A., Lamsal, L. N., Liu, Y., Lu, Z., Martin, R. V., Pfister, G. G., Pinder, R. W., Salawitch, R. J., and Wecht, K. J.: Emissions estimation from satellite retrievals: A review of current capability, Atmospheric Environment, 77, 1011 – 1042, https://doi.org/https://doi.org/10.1016/j.atmosenv.2013.05.051, http://www.sciencedirect.com/science/article/pii/S1352231013004007, 2013.

Torres, O., Bhartia, P. K., Jethva, H., and Ahn, C.: Impact of the ozone monitoring instrument row anomaly on the long-term record of aerosol products, Atmospheric Measurement Techniques, 11, 2701–2715, https://doi.org/10.5194/amt-11-2701-2018, https://amt.copernicus.org/articles/11/2701/2018/, 2018.

Valin, L. C., Russell, A. R., and Cohen, R. C.: Variations of OH radical in an urban plume inferred from NO_2 column measurements, Geophysical Research Letters, 40, 1856–1860, https://doi.org/10.1002/grl.50267, http://dx.doi.org/10.1002/grl.50267, 2013.

van Geffen, J., Boersma, K. F., Eskes, H., Sneep, M., ter Linden, M., Zara, M., and Veefkind, J. P.: S5P/TROPOMI NO_2 slant column retrieval: method, stability, uncertainties, and comparisons against OMI, Atmospheric Measurement Techniques Discussions, 2019, 1–33, https://doi.org/10.5194/amt-2019-471, https://www.atmos-meas-tech-discuss.net/amt-2019-471/, 2019.

Varon, D. J., Jacob, D. J., McKeever, J., Jervis, D., Durak, B. O. A., Xia, Y., and Huang, Y.: Quantifying methane point sources from fine-scale satellite observations of atmospheric methane plumes, Atmospheric Measurement Techniques, 11, 5673–5686, https://doi.org/10.5194/amt-11-5673-2018, https://amt.copernicus.org/articles/11/5673/2018/, 2018.

Wren, S. N., McLinden, C. A., Griffin, D., Li, S.-M., Cober, S. G., Darlington, A., Hayden, K., Mihele, C., Mittermeier, R. L., Wheeler, M. J., Wolde, M., and Liggio, J.: Aircraft and satellite observations reveal historical gap between top–down and bottom–up CO2 emissions from Canadian oil sands, PNAS Nexus, 2, pgad140, https://doi.org/10.1093/pnasnexus/pgad140, https://doi.org/10.1093/pnasnexus/pgad140, 2023.

Zhang, J., Moran, M. D., Zheng, Q., Makar, P. A., Baratzadeh, P., Marson, G., Liu, P., and Li, S.-M.: Emissions preparation and analysis for multiscale air quality modeling over the Athabasca Oil Sands Region of Alberta, Canada, Atmospheric Chemistry and Physics, 18, 10 459–10 481, https://doi.org/10.5194/acp-18-10459-2018, https://www.atmos-chem-phys.net/18/10459/2018/, 2018.

935 Zoogman, P., Liu, X., Suleiman, R., Pennington, W., Flittner, D., Al-Saadi, J., Hilton, B., Nicks, D., Newchurch, M., Carr, J., Janz, S., Andraschko, M., Arola, A., Baker, B., Canova, B., Chan Miller, C., Cohen, R., Davis, J., Dussault, M., Edwards, D., Fishman, J., Ghulam, A., González Abad, G., Grutter, M., Herman, J., Houck, J., Jacob, D., Joiner, J., Kerridge, B., Kim, J., Krotkov, N., Lamsal, L., Li, C., Lindfors, A., Martin, R., McElroy, C., McLinden, C., Natraj, V., Neil, D., Nowlan, C., OŚullivan, E., Palmer, P., Pierce, R., Pippin, M., Saiz-Lopez, A., Spurr, R., Szykman, J., Torres, O., Veefkind, J., Veihelmann, B., Wang, H., Wang, J., and Chance, K.: Tropospheric emissions: Monitoring of pollution (TEMPO), Journal of Quantitative Spectroscopy and Radiative Transfer, 186, 17–

940 39, https://doi.org/10.1016/j.jqsrt.2016.05.008, https://www.scopus.com/inward/record.uri?eid=2-s2.0-84977598074&doi=10.1016%2fj.jqsrt.2016.05.008&partnerID=40&md5=70120b28d97691037fe0e438ec7fa686, cited By 75, 2017.
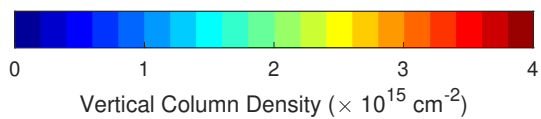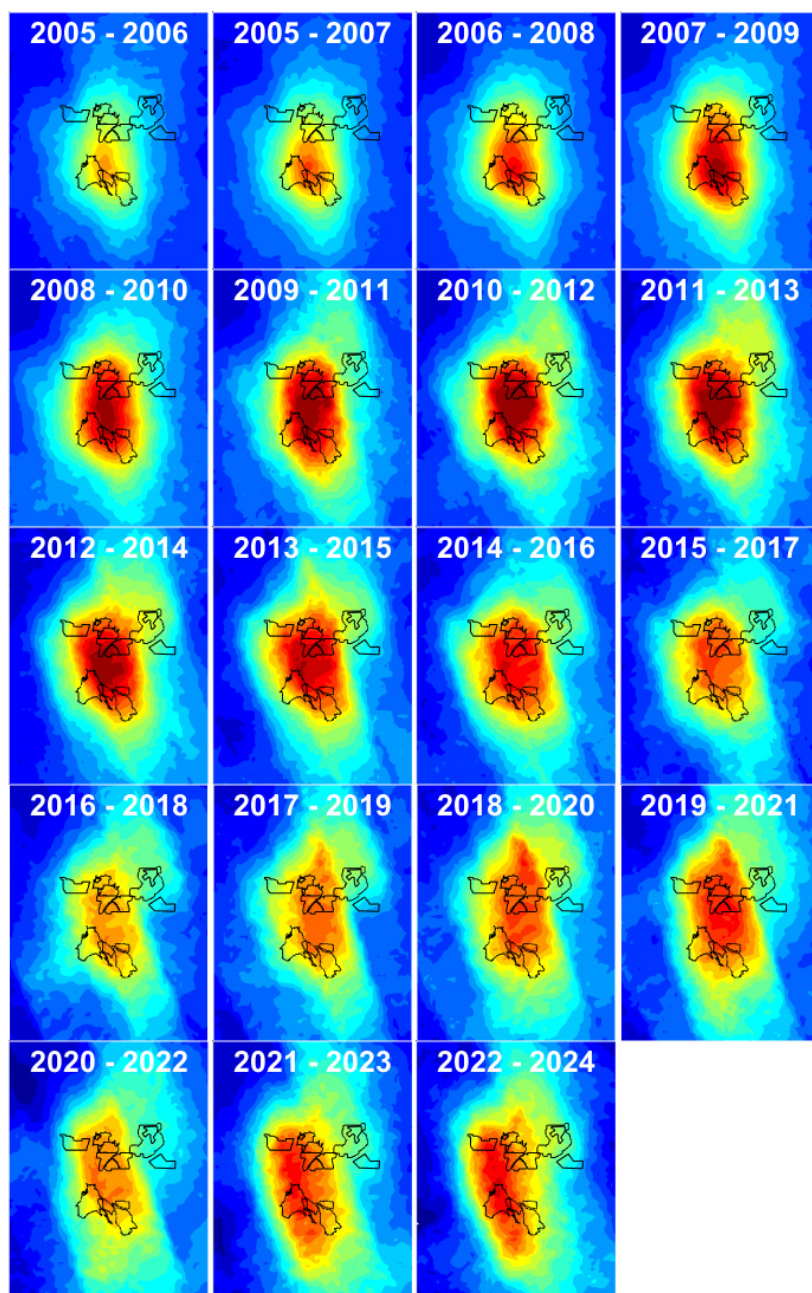
Figure D2. Three year mean OMI NO$_2$ vertical column densitiy (VCD) distributions over the surface mining. An averaging radius of 12 km was used.
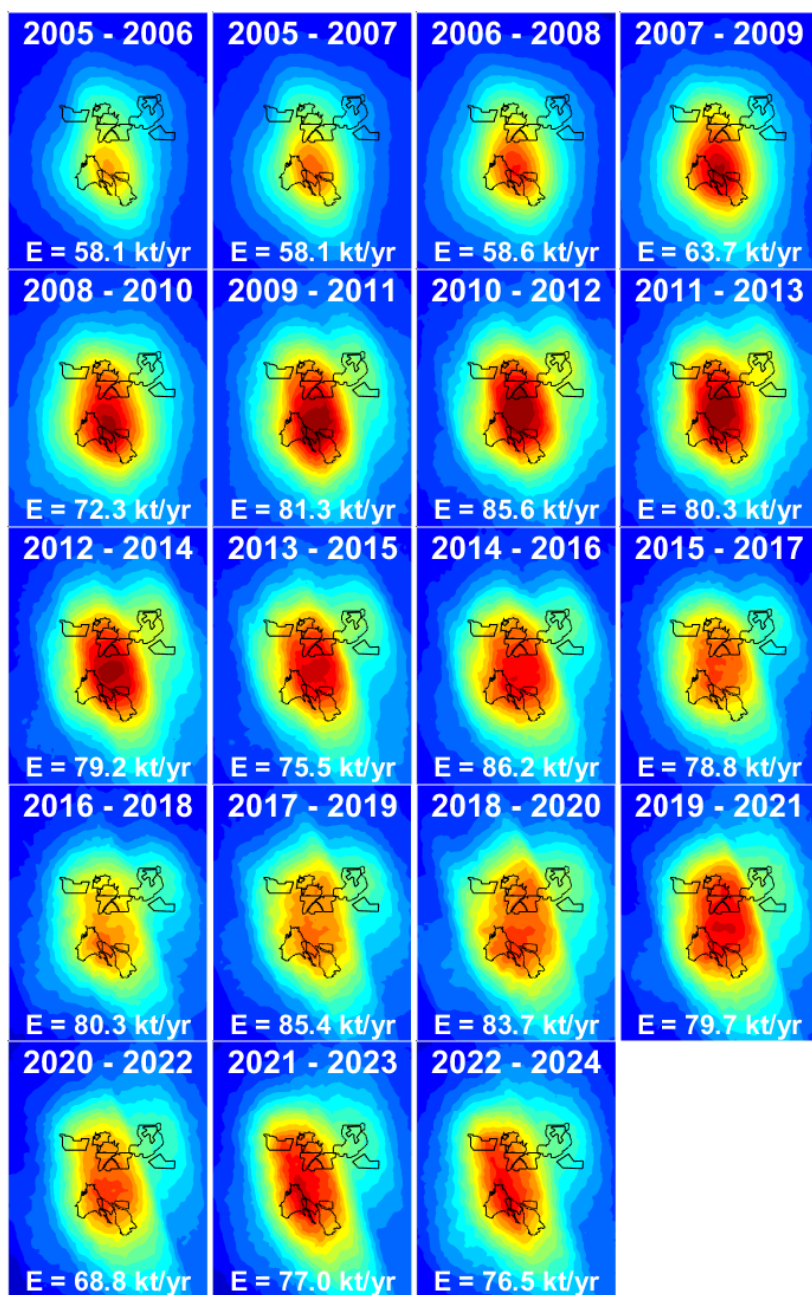
Figure D3. Three year OMI NO$_2$ vertical column densitiy (VCD) fit reconstructions over the surface mining, corresponding to the maps in Figure D2. An averaging radius of 12 km was used. The OMI-derived total NO$_x$ emissions are indicated.
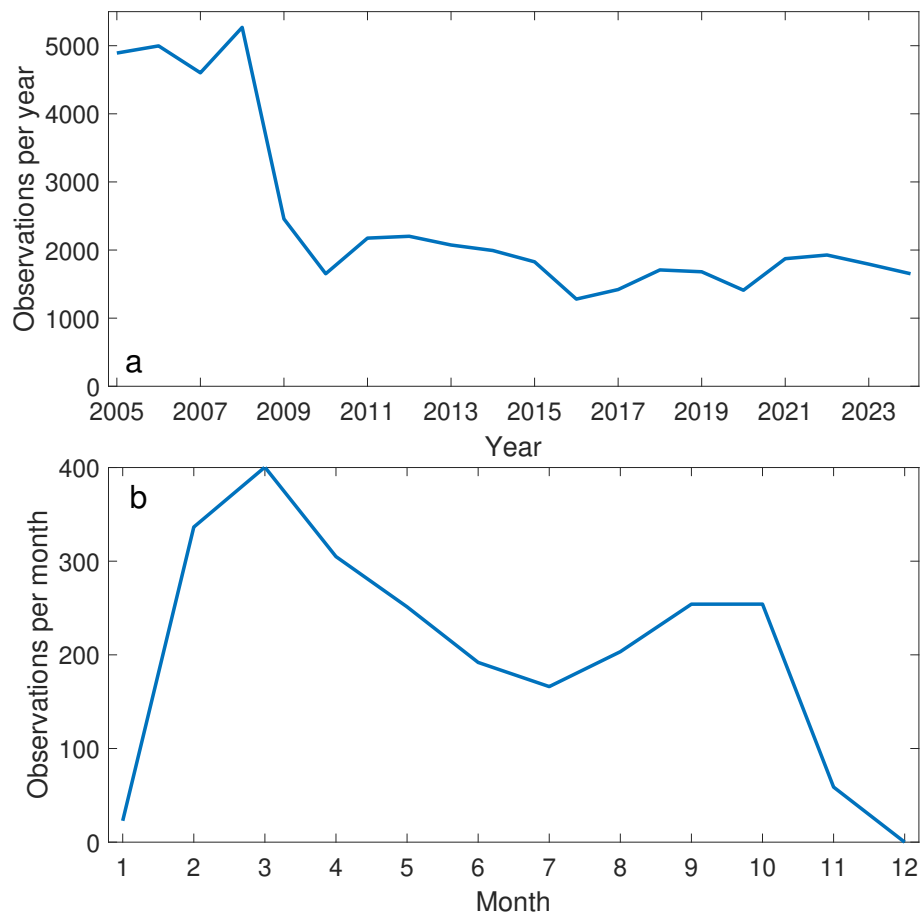
Figure E1. OMI pixels within 80 km of the reference location used in the emissions calculations: (a) Total number of per year, (b) Average number of OMI pixels (per month).
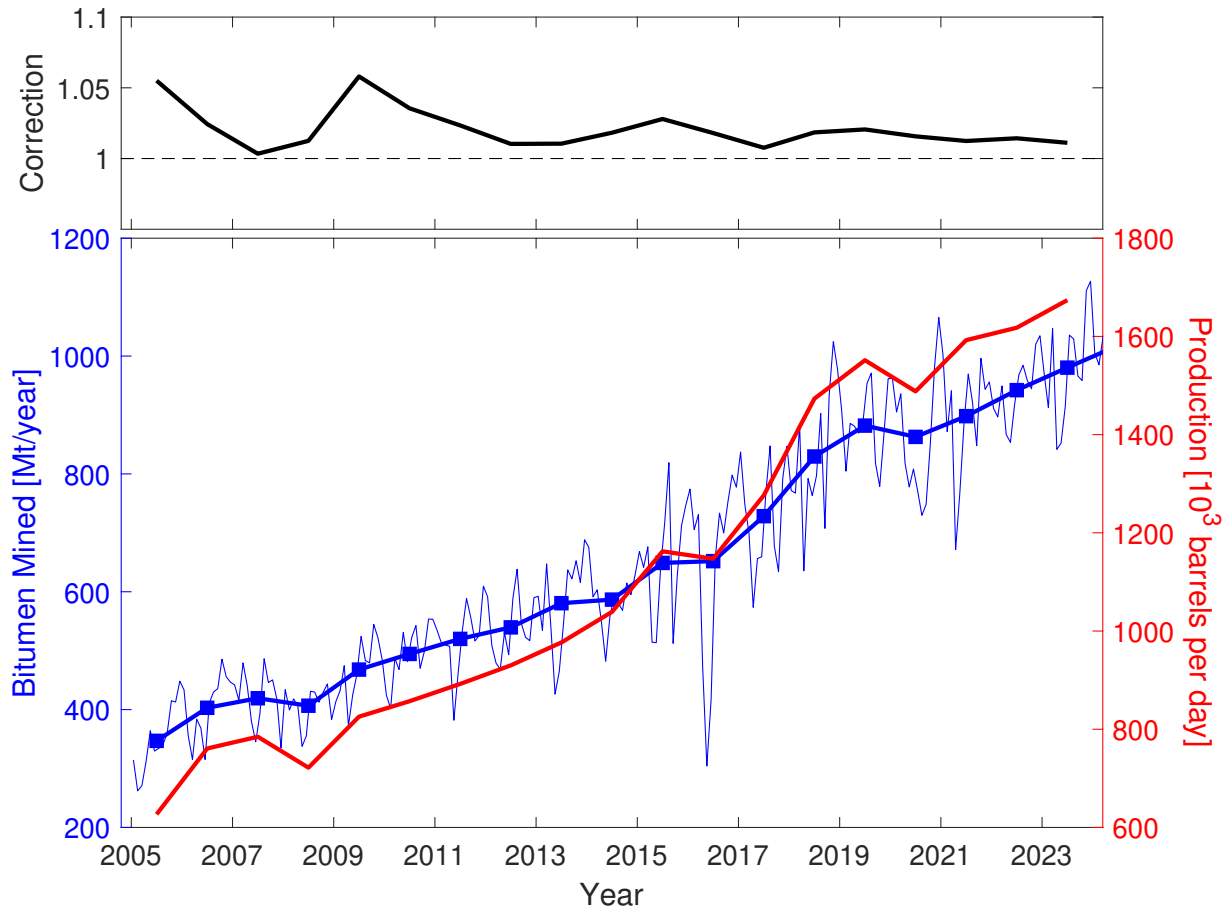
Figure E2. Total monthly and annual bitumen mined from the the surface mining region, and total production of synthetic crude from the surface mines. (The monthly bitumen mined has been converted to annual rates.) The panel at the top shows the correction factor applied to the annual emissions to account for the monthly sampling.
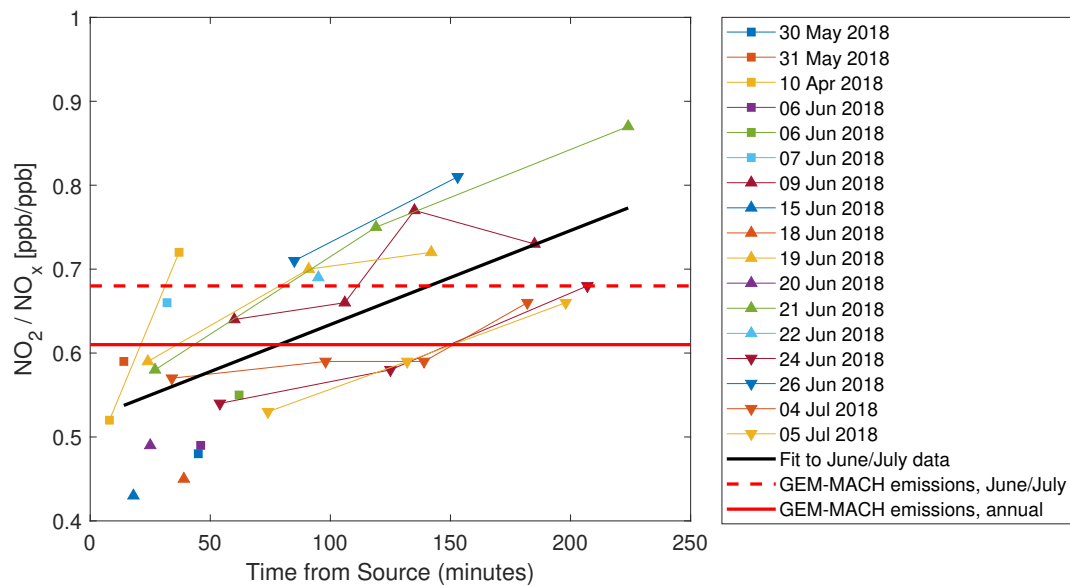
Figure E3. Comparison of NO$_2$–NO$_x$ ratios. Data from 8 flights in June and July 2018 taken during the oil sands aircraft campaign as a function of time downwind of the source, along with a fit. For comparisons, the red lines show the values using the emissions-based approach (see section 2.4.3) based on GEM-MACH model simulated OMI data. The standard deviation of the aircraft data about the line of best fit is 0.07, or 11%.
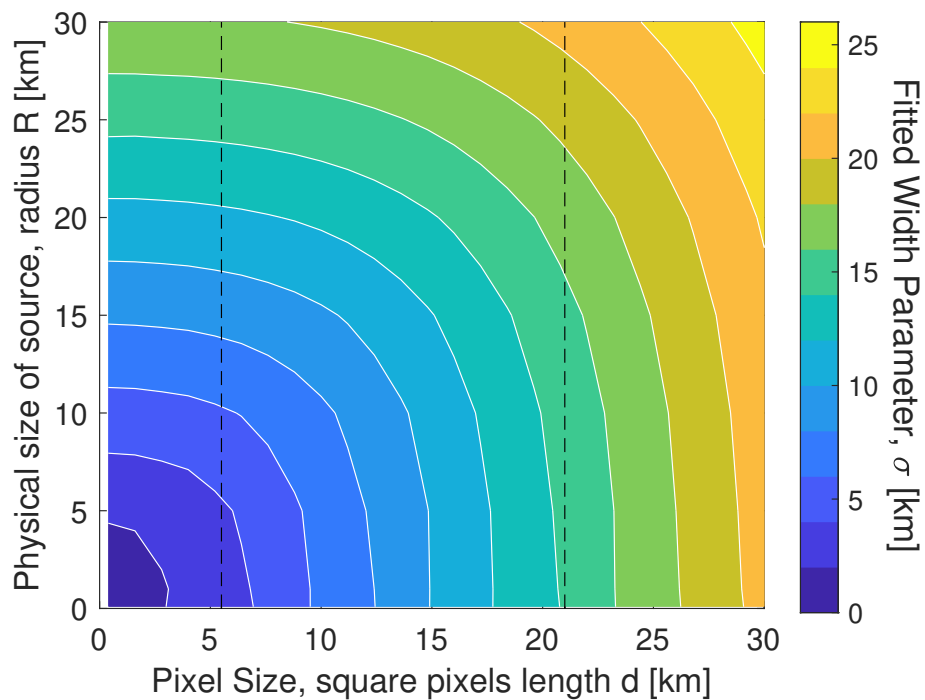
Figure F1. The relationship between the EMG width parameter, σ, and the physical extent of the emissions source and the satellite spatial resolution. See text for information on how this figure was derived. The vertical lines correspond to effective pixel sizes for the OMI and TROPOMI instruments, at 21 and 5.5 km, respectively.
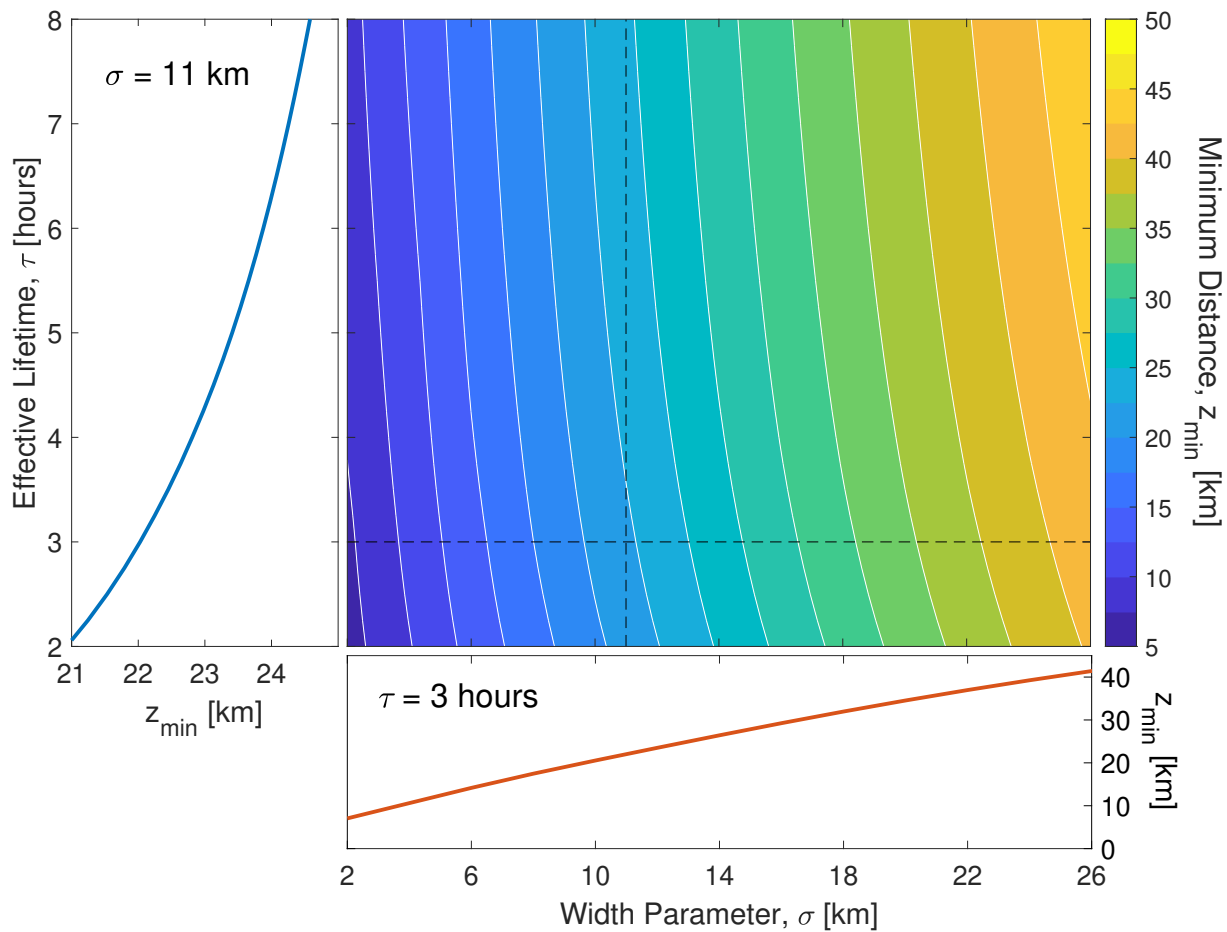
Figure F2. Minimum distance required to distinguish between two point sources as a function of plume width and effective lifetime. The line plots to the left and below show this quantity for $\sigma = 11$ km and $\tau = 3$ hours, respectively, and are cross-sections indicated by the white dashed line.
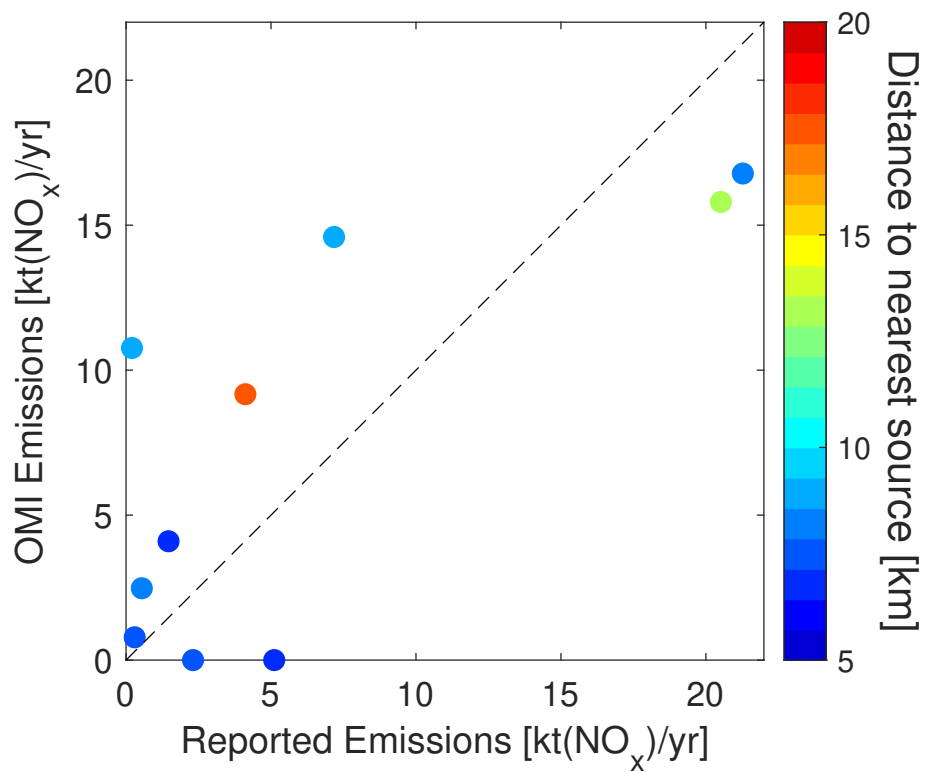
Figure F3. Comparison of reported and OMI-derived NO$_x$ emissions derived for individual mining operations considering the years 2010–2020, colour-coded according to proximity the their nearest neighbour.